

# Universidad de Alcalá

## Escuela Politécnica Superior

Grado en Ingeniería en Sistemas de Telecomunicación



### Trabajo Fin de Grado

Design and construction of a VLF monitoring station for solar  
flare detection

ESCUELA POLITECNICA

**Autor:** Alberto García Merino

**Tutor/es:** Antonio Guerrero Ortega  
Consuelo Cid Tortuero



To my parents,  
for encouraging me to  
pursue a higher education



# Contents

<b>1</b>	<b>Acknowledgements</b>	<b>i</b>
<b>2</b>	<b>Abstract</b>	<b>ii</b>
<b>3</b>	<b>Abstract (Spanish)</b>	<b>ii</b>
<b>4</b>	<b>Keywords</b>	<b>ii</b>
<b>5</b>	<b>Extended summary</b>	<b>iii</b>
<b>6</b>	<b>Glossary of acronyms and abbreviations</b>	<b>v</b>
<b>7</b>	<b>Report</b>	<b>1</b>
7.1	Introduction . . . . .	1
7.2	Overview of solar activity . . . . .	2
7.2.1	Flares . . . . .	2
7.3	The ionosphere . . . . .	3
7.3.1	Disturbances . . . . .	4
7.3.2	Propagation theory . . . . .	5
7.3.3	Wave-Hop theory . . . . .	7
7.4	The scenery . . . . .	8
7.5	Antenna design . . . . .	11
7.5.1	Selection of the antenna type . . . . .	11
7.5.2	Small loop analysis . . . . .	12
7.5.3	Radiation pattern of a small magnetic loop . . . . .	13
7.5.4	Geometry of a small loop . . . . .	15
7.5.5	Electrical model of a small magnetic loop . . . . .	18
7.5.6	Maximizing the SML SNIR . . . . .	23
7.6	Physical build . . . . .	25
7.7	Circuitry . . . . .	26
7.7.1	Preamplifier . . . . .	30

7.7.2	Power supply . . . . .	32
7.8	Measurements . . . . .	34
7.9	Data processing . . . . .	35
7.9.1	Plotter script . . . . .	39
7.10	Results and conclusion . . . . .	48
<b>8</b>	<b>Blueprints and diagrams</b>	<b>50</b>
<b>9</b>	<b>Budget and bill of materials</b>	<b>56</b>
<b>10</b>	<b>User manual and setup guide</b>	<b>59</b>
10.1	Hardware . . . . .	59
10.2	Software . . . . .	60
<b>11</b>	<b>Apendix 1</b>	<b>63</b>

## List of Figures

1	GOES X-ray flux . . . . .	3
2	Layers of the ionosphere . . . . .	4
3	Ionogram showing the electron density profile from Tromsø Geophysical Observatory . . . . .	5
4	Refraction depiction . . . . .	6
5	True ray path on the ionosphere . . . . .	6
6	Different wave-hop modes . . . . .	8
7	Received field . . . . .	9
8	VLF antenna in Anthorn, Google 2010 . . . . .	10
9	Station distribution map . . . . .	10
10	SML drawing . . . . .	12
11	SML radiation pattern . . . . .	14
12	Radiation pattern for two orthogonal SML antennas . . . . .	15
13	Effect of ground on the radiation pattern . . . . .	16

14	Area vs. number of sides for single turn loops with 10 m perimeter	17
15	Area vs. number of sides for multi turn loops with 10 m total perimeter	18
16	Electrical model of a small magnetic loop	19
17	Loop radiation resistance vs. its perimeter in $\lambda$ as given by Krauss	20
18	AC resistance of a wire with different radii	21
19	Simulation of the model with the theoretical approximation	23
20	Noise temperature vs. frequency graph given by the ITU on P.372	25
21	Antenna structure	27
22	Coil windings	28
23	Simplified block diagram of the complete system	29
24	Connection diagram	29
25	Transfer function of the filter	31
26	Amplifier PCB	32
27	Linear power supply topology	33
28	Power supply PCB	33
29	Measurements obtained during the 8 <sup>th</sup> of June	34
30	Measurements obtained during the 11 <sup>th</sup> of June	35
31	GBZ raw data captured on the 8 <sup>th</sup> of June	36
32	Digital processing system	36
33	FIR impulse response by the window method	37
34	Transfer functions of the digital filters	38
35	Intermediate steps	38
36	Processed data	39
37	Custom filtered data obtained during the 8 <sup>th</sup> of June	49
38	Preamplifier PCB	53
39	Top layer	53
40	Bottom layer	53
41	Placement	53
42	Power supply PCB	55

43	Top layer . . . . .	55
44	Bottom layer . . . . .	55
45	Placement . . . . .	55
46	Amplifier and supply setup . . . . .	59
47	Transformer . . . . .	59
48	Log captured in the 6 <sup>th</sup> of May . . . . .	63

## List of Tables

1	VLF station list . . . . .	11
2	Budget . . . . .	56
3	Materials . . . . .	57
4	PCB construction . . . . .	58
5	Antenna structure construction . . . . .	58
6	Professional fees . . . . .	58
7	Software amortization . . . . .	58
8	Hardware amortization . . . . .	58

## List of blueprints

1	Preamplifier simulation schematic . . . . .	50
2	Preamplifier design schematic . . . . .	51
3	Preamplifier PCB layers . . . . .	52
4	Power supply design schematic . . . . .	53
5	Power supply PCB layers . . . . .	54



# 1 Acknowledgements

Time passes so fast now. Without noticing I'm at the end of the telecommunications engineering degree I started back in 2015. While polishing the final details and wording of this document, I can't help but look back to all that has happened and has brought me where I am today, but most importantly, to all the people who have guided me during these years. This project is also a bit yours.

To my parents, for transmitting me the importance of an education and that hard work pays off. For encouraging me to pursue my interests even when they couldn't understand them. For giving me a stable environment where I could develop myself.

To Carlos, for teaching me things only experience could offer. For guiding me through the early days of discovering electronics when I had no idea what I was doing and, most importantly, for advising me to get into telecommunications engineering. You weren't wrong, I like it a lot.

To Miguel, with who I share great interests, for transmitting me the enthusiasm and appreciation for science I have today. To my technology teachers, who always answered any questions I could make up and thought me more than what was required.

To Borja, Paula, Emi and Miguel, who I've known for as long as I remember. For making out of high school a memorable experience and treating me as a friend even when i didn't deserve it.

To Álvaro, Fernando, Luis and Victor, for teaching me to take things seriously and make the most out of this four years without falling into apathy or laziness. You've shown me the correct path.

To Consuelo, Antonio and the Space Weather research group, for letting a couple of first graders to take on a project for which they didn't have the technical skills, but were eager to learn about.

And, of course, to the carpenter whose work is featured in this project. For creating a masterpiece that has given this project a lot of value.

To all of you, thank you.

## 2 Abstract

Understanding solar activity is now more important than ever. Flares and coronal mass ejections (CMEs) can produce devastating effects in our technology and disrupt telecommunications. Ways of monitoring it have been developed, but rely on extremely complex and expensive equipment. Since 1936, very low frequency (VLF) monitoring is known to allow flare detection through events called sudden ionospheric disturbances (SIDs) produced by the change on hard X-ray flux in the Earth's ionosphere, which is a much more simpler and accessible method. This project aims to provide the theoretical background and design for one of this monitoring stations, along with its construction and a demonstration.

## 3 Abstract (Spanish)

Entender la actividad solar es ahora más importante que nunca. Tanto fulguraciones como eyecciones de masa coronal (CMEs) pueden producir efectos devastadores sobre nuestra tecnología además de interrumpir las telecomunicaciones. A pesar de que ya existen equipos dedicados a su monitorización, estos son extremadamente complejos y costosos. Desde 1939 se ha podido utilizar la monitorización de transmisiones de muy baja frecuencia (VLF) distantes para la detección de fulguraciones solares, a través de las perturbaciones ionosféricas súbitas (SIDs) producidas por el cambio en el flujo de rayos X duros en la ionosfera; un método mucho más sencillo y accesible. Este proyecto tiene como objetivo desarrollar los fundamentos teóricos y proponer un diseño de una de estas estaciones de monitorización junto con su construcción y prueba.

## 4 Keywords

Space Weather, Flare, X-Rays, Ionosphere, Disturbance, Propagation, VLF, Antenna, Logger.

## 5 Extended summary

Solar activity has gain importance since the last century. With the current use of technology and telecommunications and our dependence of them, events such as the Carrington event would have devastating consequences. However, as our systems get more complex and linked together, weaker events can still have serious consequences.

In general, solar activity is being monitored in several ways. In the case of flares mainly direct ways of measuring them have been used. These include the GOES satellites. However, since 1936 a method of measuring them by monitoring the effects on the propagation of radio waves emitted by distant very low frequency (VLF) transmitters has been developed. It is based on the changes that are produced on the lowest ionospheric layers due to variations in the ionization profiles. When a hard X-ray flare occurs, a phenomenon named sudden ionospheric disturbance takes place. This produces changes to the received field's amplitude and phase, which can be measured by a receiving station.

VLF radio waves are known to benefit from ionospheric propagation. This, added to the fact that they feature relatively low attenuation in water have made them ideal candidates for submarine and non line of sight communications around the globe. For this reason, they were extensively used and researched during the 20<sup>th</sup> century, specially during World War II (WWII).

These type of waves propagate through the Earth-ionosphere waveguide, in a phenomenon called multi hop propagation. This allows to describe the receiving field as the summation of the different modes which are characterized by the number of reflections they experience in the ionosphere. As each of these ionospheric modes and the ground wave propagate through different paths, the addition in the receiving end will produce what is called modal interference. As a result, the receiving field will change in phase and amplitude depending on the ionospheric conditions along the path.

This idea has already been developed in numerous stations as it is not a new subject. Luckily, the use of already existing transmitters, devoted to submarine communications, is possible. The receiver itself is usually built around either a loop antenna or a monopole. In this case a small magnetic loop antenna is used, which couples to the magnetic field following Faraday's law of electromagnetic induction. This essentially produces an alternating voltage at the leads of the coil which depends on the variation of the receiving field.

Being able to transform the incoming waves into a potential at the coil ends allows to sample it using commercial audio equipment such as a computer audio card. This is possible as these frequencies mostly fall right into the standard audio spectrum, approximately from 10 kHz to 24 kHz, though transmissions at higher frequencies also exist. For these, specific sound cards used in professional setups are needed. However, the signal levels coming out of the antenna are weak, and can not be sampled directly.

The signal conditioning is done using a simple preamplifier with active filtering and gain control, and its dedicated power supply, for which a design is proposed. This allows to send the signal over several tens of meter long cables without significant degradation and to adapt the levels to the range the sound card accepts.

A computer can then be set up with the open source software SuperSID,

which transforms to the frequency domain and logs the data through time.

Noise and interferences are also a major issue in this frequency range, which makes it mandatory to find a quiet location away from printers, screens and switching power supplies. However, as a way of mitigating this to some extent, a digital processing system has been developed which allows to filter out periodic intrusions in the logged frequency band by nearby appliances.

Finally, the correct operation of the system can be verified by recording the ionospheric day-night cycle. This is produced by the change in the flux of ionizing radiation as the incidence angle over the ionosphere changes when the Sun travels through the sky. From this cycle, the sunrise and sunset can be distinguished, as well as a concave curve during the day with its maxima at local noon.

## 6 Glossary of acronyms and abbreviations

- **CME** Coronal Mass Ejection
- **HF** High Frequency
- **VLF** Very Low Frequency
- **SID** Sudden Ionospheric Disturbances
- **UV** Ultra Violet
- **EIW** Earth Ionosphere Waveguide
- **ITU** International Telecommunication Union
- **WWII** World War II
- **SNIR** Signal to Noise and Interference Ratio
- **SML** Small Magnetic Loop
- **NEC** Numerical Electromagnetics Code
- **DC** Direct Current
- **AWG** American Wire Gauge
- **AC** Alternating Current
- **SNR** Signal to Noise Ratio
- **BER** Bit Error Rate
- **RMS** Root Mean Square
- **PC** Personal Computer
- **FFT** Fast Fourier Transform
- **SFTP** Secure File Transfer Protocol
- **GBW** Gain Band Width
- **PCB** Printed Circuit Board
- **FIR** Finite Impulse Response
- **THT** Through Hole Technology
- **SMD** Surface Mount Device
- **OPAMP** Operational AMPlifier
- **DIP** Dual In line Package
- **AMP** AMPlifier
- **SSH** Secure SHell

## 7 Report

### 7.1 Introduction

Auroras are the kind face of solar activity. Usually appreciated for their beauty as a natural light show, it is not often known that they are produced by the interaction of solar wind with the Earth's magnetosphere. Without the development of technology and telecommunications this is all we would be able to see, as no further effects could be detected. This changed with the development of telecommunications, which started with the deployment of telegraphic systems in the 19th century.

In 1859 [1], Carrington and Hodgson witnessed a "remarkable phenomenon". In its report to the Royal Astronomical Society, Carrington described seeing a very bright flash of light in the Sun. A flare. A few days later, a CME associated to that flare hit the Earth, producing the malfunctioning of telegraph lines, as well as some strange phenomena. Several operators even reported being able to transmit without power. Today, we know this as the Carrington event.

A lot has changed since then. Nowadays we greatly depend on much more complex systems in an increasingly technological world. Telecommunications are now more than ever key to our society and extreme events such as the Carrington event would have a devastating effect today. However, as our technology advances, and we depend more and more on it, weaker events can also produce severe consequences. This was recently proven during the Atlantic hurricane season of 2017 as in September, in the aftermath of hurricane Irma in the Caribbean region, first responders lost high frequency (HF) communication after a series of X class flares reached the Earth [2].

As prediction of solar flares and CMEs is still a difficult subject the solution currently goes through more research and constant monitoring of solar activity. There are already systems that measure the solar X-ray flux, such as the GOES satellites, but measuring X-ray flux directly can have several drawbacks. First, it is necessary to use satellites, as the atmosphere blocks radiation at those ranges. This makes it extremely expensive when compared to systems like the one proposed in this project. Additionally, as radiation is measured directly, the sensors can saturate during severe events.

While the proposed system may not provide the same degree of accuracy as the ones described, it can provide complementary information during these events. Due to its working principle, the detection of solar flares is done indirectly and is only available during local day. This is because the system will measure changes in the lowest region of the ionosphere through monitoring incoming radio waves from distant very low frequency (VLF) transmitters. As these changes are produced by variations in the hard X-ray flux, which result in sudden ionospheric disturbances (SIDs), the intensity of the flare can be inferred.

Due to its simplicity it can be built by anyone with a few technical skills, and deployed anywhere. And by using several stations and monitoring several transmitters, maps of the ionospheric conditions can be made.

## 7.2 Overview of solar activity

The Sun is an active star which is constantly emitting electromagnetic radiation and particles. In regards to radiation, it can be modeled approximately as a black body radiator. Even if the visible spectrum predominates, radio, X-rays and other types of electromagnetic radiations are also being produced. This provides a constant stream of ionizing and non ionizing radiation. However, more circumstantial events are not constant through time.

The number of sunspots and the latitude where these spots appear follows a 11 year cycle. Flares are more common during the years with more sunspots. This makes it possible to differentiate between low activity periods and high activity ones, named solar minimum and solar maximum. As the Sun is currently close to the minimum in this cycle, not much activity is expected.

Active regions are convulse places on the Sun where flares and other types of solar emissions tend to occur. As the sun rotates, even if it does it at different rates depending on latitude, these regions will move over the Sun's surface, entering and leaving the visible solar disk (the side of the Sun visible from Earth). As a consequence, events can have a varying impact on Earth depending on their intensity and whether they are facing the Earth or not.

The basics of solar flares are laid out in the next section, as having a minimum understanding about this type of phenomena is required for the development of this project.

### 7.2.1 Flares

Flares are a type of solar emissions where electromagnetic energy is released [3]. They can be defined as a localized brightening of the Sun, involving a wide range of the electromagnetic spectrum. This provides a classification depending on the type spectral emission, from flares only involving radio waves to other types where X-rays are also emitted along with other types of radiation.

For flares which contain X-rays, a scale has been developed attending to the measured X-ray flux. The scale assigns a letter A, B, C, M or X to indicate the flare intensity, with A being the weakest flare and X the strongest. This logarithmic scale is usually given with an accompanying number from 1 to 9 (e.g. C7.3, X4.7) except for X class flares, which it isn't limited. This number is related to the X-ray flux in the channel 1-8 Å. An example of the X-ray flux measured by the GOES satellites featuring several B and C class flares is shown in figure 1.

Several phases can be distinguished during a flare: preflare, impulsive, flash and decay. During the first phase a sudden release of hard X-rays and microwaves are produced in the solar corona. It is this phase the one of interest to this project. Then, an increase in UV and soft X-rays is produced in the chromosphere during the impulsive phase. During the flash and decay phases, other emissions enter into play. While the duration of each phase varies greatly, the impulsive phase lasts several minutes and the total event can last several hours.

Large flares are an indicator that a CME may be coming as in some cases they can be associated [3]. This serves as an early warning system for other

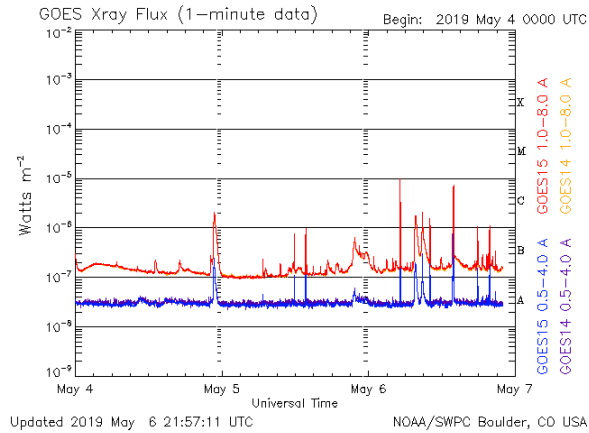


Figure 1: GOES X-ray flux

types of disturbances as CMEs can take from hours up to several days to reach the Earth, while flares need only minutes.

### 7.3 The ionosphere

The Earth’s atmosphere can be stratified into several layers with different characteristics. Among them, the ionosphere [4] spans approximately from heights of 40 km to 2000 km though it is usually bounded between 90 km and 1000 km. This layer receives its name from the ions that are produced by the Sun’s radiated energy, which is of high interest for telecommunications due to its electrical characteristics.

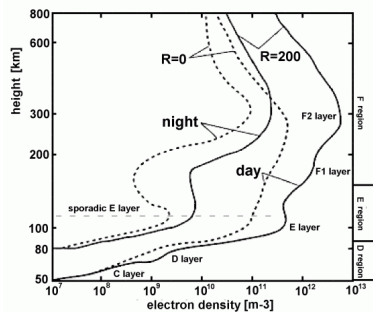
The ionization is produced when the high energy radiation coming from the sun rips off electrons from the atoms. Because of this, only positive ions can be found, as the net charge of the atoms is not neutral due to the greater number of protons than electrons. As a result plasma is produced, a medium where electrons move freely, giving a high conductivity to the layer.

Given its high conductivity, this layer is of special interest for telecommunications as it enables non line of sight communications across the globe. The operating principle is the reflection of low frequency radio waves, which will be further analyzed in section 7.3.2.

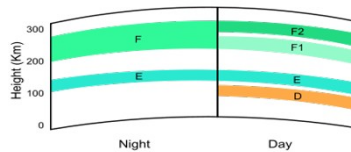
Though it is easier to think about the ionosphere as a constant and homogeneous layer this is far from reality. Its properties vary with height and time, as the ionization levels change with the solar radiation incidence angle as well as with solar activity. A way to characterize the ionosphere is by calculating the electron density vs. height profile as shown in figure 2a. This is done with ionosondes, which transmit a range of frequencies to the zenith and listen for the reflections. Knowing which frequencies reflect at every height, the electron density profile can be computed. An example ionogram is shown in figure 3.

By observing the maxima in the electron density profile, several layers can be identified. These are (figure 2b): the E and F layers during night and the D,





(a) Electron density profile from INGV - Istituto Nazionale di Geofisica e Vulcanologia



(b) Schematic view of the ionosphere from Wikimedia Commons

Figure 2: Layers of the ionosphere

E, F1 and F2 layers during the day. Their names come from the E layer, which was the first layer to be discovered and was named with the letter 'E' for its 'Electric' properties. As expected, the electron density profile, and consequently the layers, change from night to day. The formation of the D layer in the lowest section of the ionosphere ( $\approx 90$  km) and a separation in the F layer can be distinguished. From these, it's the D layer the one of our interest as it'll be discussed in section 7.3.1.

As mentioned before, the Sun is approximately a black body radiator, which means that it radiates electromagnetic energy at (almost) all frequencies. Even though it peaks at the visible range of the electromagnetic spectrum, it is also constantly emitting ionizing radiation above the ultra violet (UV) range.

The D layer, being the lowest layer of the ionosphere, is ionized by high energy electromagnetic radiation, as it can penetrate deeper into the ionosphere. Therefore, while UV radiation ionizes the E layer, they are the Lyman  $\alpha$  radiation from the emission of hydrogen atoms and the hard X-rays the sources of ionization of the D layer, as they are highly energetic and can penetrate deeper into the ionosphere.

### 7.3.1 Disturbances

The black body nature of the Sun, provides a constant stream of ionizing radiation to the ionosphere while illuminated in the form of X-rays and Lyman  $\alpha$  radiation. However, sudden changes in the received radiation can provide timely boosts to the electron density of the ionosphere. These phenomena are named Sudden Ionospheric Disturbances (SIDs) and can be produced by solar flares.

When looking at the D layer, the stream of hard X-rays is indirectly measured [5]. This means that when a flare containing hard X-rays reaches the Earth, due to their impulsive nature, a sudden enhancement of the electron density will occur.

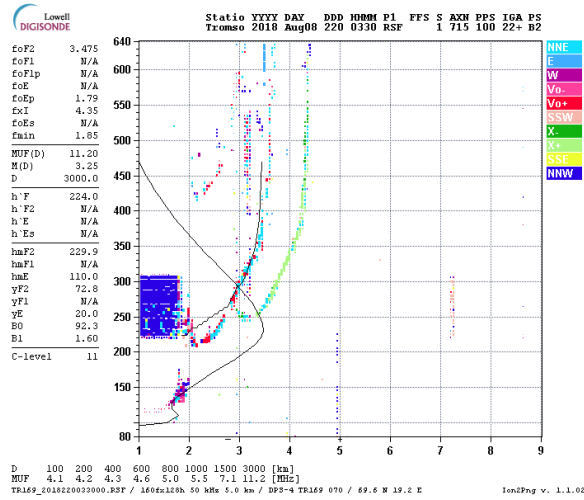


Figure 3: Ionogram showing the electron density profile from Tromsø Geophysical Observatory

### 7.3.2 Propagation theory

It is well known that very low frequencies (VLF) can be used to communicate over extremely long distances. For this reason they were used and researched during the 20<sup>th</sup> century as the basic form of military communication. The reason for this is that the ionosphere serves as a reflector for this specific frequency range, making it possible to create non line of sight over the horizon radio links. Though it is not our case of study, it is interesting to know that these waves can penetrate the water up to depths of approximately 20 meters, which is useful to maintain communication with submarines.

Although it is commonly considered that waves suffer a total reflection on the ionosphere, what happens in fact is a refraction which curves the ray and makes it go back to the Earth surface, as depicted on figure 5. The reasoning can be easily followed using Snell's law, which is shown in equation 1, and figure 4 as a reference. In our case, analyzing for differential of  $z$ , for a ray going away from the Earth's surface to curve and return the condition  $\theta_2 > \theta_1$  must be satisfied. If not, without considering absorption in the ionosphere, the ray would scape the Earth. As a consequence of this, the refraction index ( $n_i$ ) of the first medium must be greater than the one of the second medium.

$$\sin(\theta_1) \cdot n_1 = \sin(\theta_2) \cdot n_2 \quad (1)$$

It can be concluded that the refraction index must decrease with height. As air in normal conditions has a refraction index that is approximately one, the ionosphere refraction index must be less than unity. This reasoning holds up when the expression for the refraction index of plasma as a function of the electron density, which is shown in equation 2, is considered.

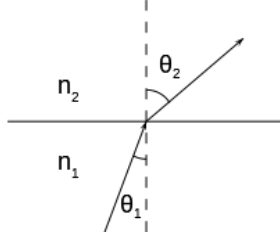


Figure 4: Refraction depiction

$$n^2 = 1 - \frac{\omega_p^2}{\omega^2} \quad (2)$$

$$\omega_p = \frac{N_e \cdot q_e^2}{\epsilon_0 \cdot m_e} \quad (3)$$

To solve this, the electron density profile of the ionosphere, which was explained in section 7.3, has to be taken into consideration. On the D layer, the lowest of the ionosphere, the electron density increased exponentially with height. This leads, according to equations 2 and 3, to a decrease of the refraction index with height given the mass of the electron ( $m_e$ ), the charge of the electron ( $q_e$ ), the electron density ( $N_e$ ), the electrical permittivity of vacuum ( $\epsilon_0$ ) and the angular frequency of the electromagnetic wave ( $\omega$ ) [6].

As a note, it is commonly thought that the refractive index can not be less than one, as it is the quotient of the the speed of electromagnetic waves in vacuum and the phase velocity of electromagnetic waves in the medium itself. However, as the phase velocity does not carry information, it can be higher than the speed of light under certain conditions.

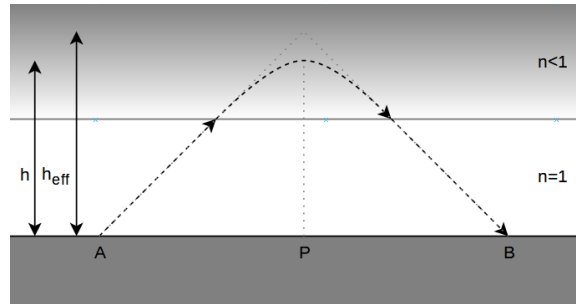


Figure 5: True ray path on the ionosphere

Though the calculation of the true ray path in the ionosphere is out of the scope of this project, an schematic depiction is shown in figure 5.

For simplicity, it is usually considered that waves suffer a specular reflection at an effective height on a perfectly reflective ionosphere concentric to a spherical Earth. The result of this assumption is the two parameter  $H'\beta$  model [7]. With

it, the effective reflection height and the sharpness of the electron density profile can be controlled. Typical values for this model are given by Wait, and are 70 km to 90 km for  $H'$  and  $0.3 \text{ km}^{-1}$  for  $\beta$  during local day.

These typical values change during the day depending of the Sun's incidence angle and solar activity. During X-rays flares, due to the increase of ionizing radiation, the reflection height will lower and the sharpness of the profile will increase. Values for  $H'$  and  $\beta$  as a function of flare intensity have been tabulated in recent papers [8].

From this  $H'\beta$  model, two methods of understanding ionospheric propagation have been developed. These consider propagation through the Earth-Ionosphere Waveguide (EIW), and are:

- Waveguide mode theory
- Wave-hop theory

Waveguide mode theory analyzes the propagation using electromagnetic mode theory. It is the preferred method for distances over 2000 km as the effects of diffraction from the curvature of the Earth have to be taken into account, but offers a more complex mathematical analysis. On the other hand, wave-hop theory offers a more intuitive approach, analog to ray theory. As it is proven [9] that wave-hop theory provides equivalent results to waveguide mode theory and due to simplicity, wave-hop theory will be used. The International Telecommunication Union (ITU) recommendation ITU-R P.684 provides a wave hop model for propagation at VLF frequencies.

### 7.3.3 Wave-Hop theory

Wave hop theory is a way of understanding ionospheric propagation as a series of rays that propagate independently and interfere with each other. It is based on geometric ray tracing of the transmitter signal and reconstructs the received signal as the addition of the ground wave and each of the ionospheric rays. These idea is expressed in equation 4 which describes the fundamentals of this model. There, the index  $n = 0$  represents the ground wave and  $n > 0$ , the ionospheric hops. For the latter, the index which shows the order of the mode, represents the number of reflections that are produced on the ionosphere by that specific mode. Therefore, a first order mode will have one ionospheric reflection while a second order one will have two. The only task left to us then is to compute each of the mode field strength vectors and combining them afterwards. A visual representation of this concept can be found in figure 6, where the first three ionospheric modes are drawn.

$$\vec{E}(d) = \sum_{n=0}^N \vec{E}_n(d) \quad (4)$$

It is intuitive that higher order modes will have less impact on the receiver as they will be greatly attenuated. Furthermore, approximately at distances over 1000 km, the ground wave features a field strength weaker than the ionospheric hops. The ITU, on its radio communication section, gives a method for analyzing radio propagation for frequencies below 150 kHz [10].

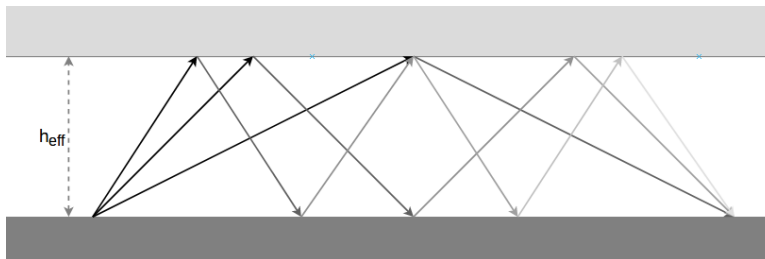


Figure 6: Different wave-hop modes

Following the procedures laid out by the ITU, the field strength at reception for each of the ionospheric modes, as well as for the ground wave [11] can be computed. At the receiving end the field strength phasors can be combined as shown graphically in 7a. Each of the modes will arrive with a different phase and amplitude, which results on a phasor from which its amplitude will be measured. This is the true purpose of our system: recording the amplitude variations of the phasor that results from the combination of the ground wave and the different ionospheric modes through the day. Performing this operation over a range of distances between the transmitter and receiver the variation on amplitude shown in figure 7b can be obtained.

An interesting effect of the addition of the phasors is that when the ionospheric conditions change, which can be described through the  $H'$  and  $\beta$  parameters, the measured amplitude can either increase or decrease. This effect is well known and has been pointed out in several papers [12] over the years.

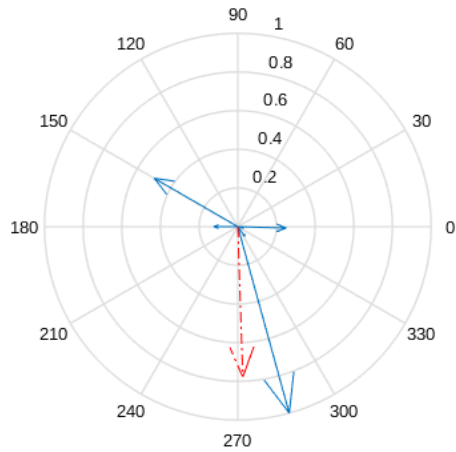
Due to the geometry of the problem only certain areas of the ionosphere are relevant. In fact, only the conditions where the hops are produced will affect the received field. In the case of really far away transmitters ( $d > 2000$  m) the ground wave will be almost non existent, which makes the interference pattern solely dependent on the first few ionospheric modes that are able to efficiently propagate. If they are closer ( $d < 2000$  m) higher order modes won't be able to propagate and the interference pattern will be determined by the ground wave and the first ionospheric hop.

There is indeed a minimum distance from which modal interference is possible, as when transmitter and receiver are too close the first mode ionospheric hop won't be able to return as it reaches the ionosphere almost perpendicular to it. Furthermore, the ground wave would be overwhelmingly strong and would mask the effect of the interference, if any.

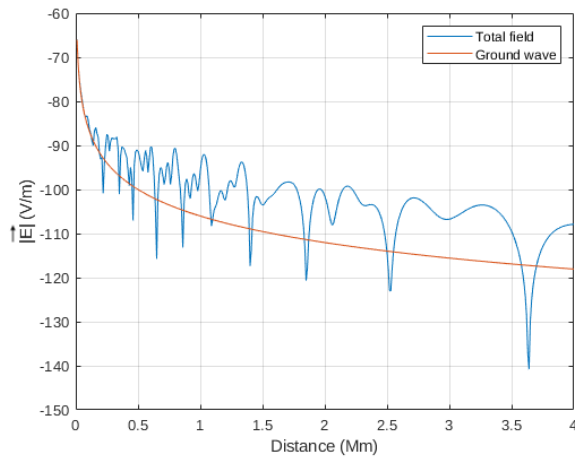
## 7.4 The scenery

The proposed system consists of a transmitter and a receiver. As the channel is the one in charge of introducing the variations to the signal depending on the solar activity, the transmitter and receiver will have passive jobs. Furthermore, only the received power will be analyzed, which means that no exchange of information is needed between them. This is an advantage, as the transmitter can be used for different tasks.

Ionospheric communications were a heavily researched topic during World



(a) Vectorial addition of ionospheric modes at the receiver. Individual ionospheric modes in blue. Total addition in red



(b) Field vs. distance

Figure 7: Received field

War II (WWII). This came out of necessity, as they allowed communications with submarines and beyond the horizon. A great number of military radio transmitters were built for this purpose and even if lots of them have been destroyed, demolished or decommissioned some are still in operation.

These transmitters are scattered around the world and as shown in figure 8, are huge structures. In the case of the Anthorn transmitter, it is composed of 13 vertical elements of 227 meters tall each. The reason for this is that antenna



Figure 8: VLF antenna in Anthorn, Google 2010

efficiency reaches reasonable levels when its elements have sizes comparable to the wavelength. For VLF frequencies, wavelengths go from few kilometers to tens of kilometers, which requires colossal antennas.

By taking advantage of the already existing transmitters that are still in operation the only job is building the receiver. Its task will be to measure the received power and log it thought the day.

It is normal for these transmitters to go down on maintenance every few weeks, so monitoring several of them is necessary for redundancy. In figure 9 several VLF transmitters are displayed over the world map, which gives an idea of how they are distributed around the world. These are listed in table 1



Figure 9: Station distribution map

A direct consequence of the distribution of the transmitters is that there will be certain regions over which the ionospheric conditions will remain unknown. Recalling the working principle of this system, only the conditions above the great circle path between transmitter and receiver can be measured. By listening to the transmitters featured in figure 9, regions above central and south America, as well as Africa are out of reach as no transmitter produces hops over them given the location of the receiver.

Call sign	Frequency (Hz)	Location
VTX1	16300	South Vijayanarayanam, India
JXN	16400	Novik, Norway
GBZ/GQD	19580	Anthorn, UK
NWC	19800	Exmouth, Australia
ICV	20270	Isola di Tavolara, Italy
NPM	21400	Pearl Harbor, Lualuahei, HI
HWU	21750	Rosnay, France
NDT	22200	Ebino, Japan
DHO38	23400	Rhauderfehn, Germany
NAA	24000	Cutler, ME
NLK	24800	Oso Wash, Jim Creek, WA
NRK/TFK	37500	Grindavik, Iceland

Table 1: VLF station list

Other consequence of the placement of the transmitter and receiver is that, as they get closer together, fewer number of modes exist along the path. The worst case is when they are too close even for the first ionospheric mode to exist. The reason for this is that the rays need a minimum angle of incidence in the ionosphere for them to return to the Earth surface.

There is little information about the specifications of these transmitters due to their military application, which makes it impossible to model the expected field intensity at the receiver. However, from the types of antennas used in these transmitters and experimentation, it is known that vertical polarization is used. This must be taken into account when designing the antenna.

## 7.5 Antenna design

The antenna is the element that converts the instantaneous field strength of the received wave to a voltage that can then be sampled and logged by the system. In this section, the theoretical background will be laid out to determine the best characteristics for the final design.

### 7.5.1 Selection of the antenna type

Common types of antennas that are used in this frequency range are monopoles (whip) antennas, dipoles and loop antennas. As it is not possible to build antennas comparable to the size of a wavelength in this frequency range, these will all belong to the so called electrically small antennas category. For reference, wavelengths in the VLF range go from several kilometers to tens of kilometers. Another distinction that can be made is the type of coupling to the incoming wave. Whip antennas and dipoles couple to the electric field of the incoming wave, while loops couple to the magnetic field.

While whip antennas and dipoles have omni directional patterns in azimuth when used for vertical polarization, loops don't. This may be seen as an advan-



tage as it allows to monitor stations from different directions and it usually is. However, it also leads to a higher level of interferences as they can be picked up from any direction. On the other hand, small loop antennas provide two sharp nulls on azimuth. These can be used to attenuate interference sources when carefully placed and are also called "deaf" sides of the antenna.

For this reasons, the so called small magnetic loop antenna has been chosen, which is commonly known as SML.

### 7.5.2 Small loop analysis

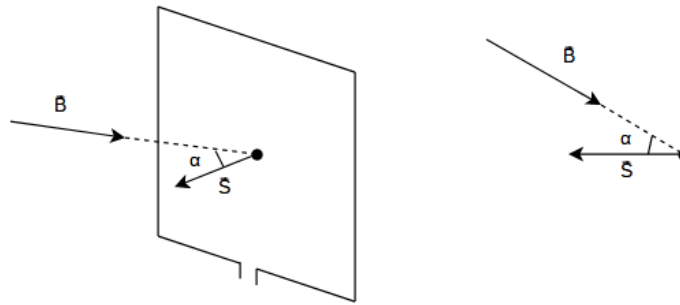


Figure 10: SML drawing

The radiation pattern for a SML can be solved using Faraday's law of electromagnetic induction, shown in equation 5. In the presence of a changing magnetic field, which in this case will be produced by the radio frequency carrier of the transmitted signal, an electromotive force proportional to the enclosed area will be induced in the leads of a looped conductor.

$$\mathcal{E} = -\frac{\partial\Phi_B}{\partial t} \quad (5)$$

When considering a small magnetic loop, the calculations are greatly simplified, as the field can be considered uniform on the area enclosed by the loop. As a result, the magnetic flux through the loop can be simplified to a multiplication. As the magnetic flux is constant in the coil surface it can be written as the dot product of the field and surface vectors. This produces an interesting dependence with the incidence angle that will be later analyzed.

$$\Phi = \iint \vec{B} \cdot d\vec{S} = \vec{B} \cdot \vec{S} = B \cdot S \cdot \cos(\alpha)$$

The complete equation can now be considered, accounting for a multi-turn loop where  $\alpha$  is the angle between the surface vector and the magnetic field

vector.

$$\mathcal{E}(t) = -\frac{\partial}{\partial t} N \cdot S \cdot B(t) \cdot \cos(\alpha)$$

Considering an incoming wave on a fixed point in space, the variation of the magnetic field can be described as a sinusoidal variation with time.

$$\begin{aligned} B(t) &= B_0 \cdot \cos(\omega t + \phi) \\ \mathcal{E}(t) &= N \cdot S \cdot \omega \cdot B_0 \cdot \sin(\omega t + \phi) \cdot \cos(\alpha) \end{aligned}$$

To reduce the number of terms, the product  $N \cdot S$  can be joined into the effective area,  $S_{eff}$ , as its terms share meaning. A single turn loop with an area equal to  $S_{eff}$  will produce the same output as a multi turn loop if  $N \cdot S = S_{eff}$ . Further implications of this idea are developed on section 7.5.6, where the loop signal to noise and interference ratio (SNIR) is discussed.

A way of enhancing the fields in an antenna, thus increasing the output level, is using a core material with a high relative magnetic permeability ( $\mu_r$ ). In the case of reasonably big loops this is unfeasible. The core will therefore be made of air.

As our interest lies on the amplitude of the signal, which dictates the modulus of the phasor, the dependence with time can be left out.

$$||\mathcal{E}|| = S_{eff} \cdot \omega \cdot B_0 \cdot \cos(\alpha) \quad (6)$$

Finally, the expression for the effective height of a small magnetic loop can be determined. This parameter measures how well an antenna converts the receiving fields into electrical signals, so it is of vital importance and has to be maximized. This task is left for section 7.5.4. It is defined as the ratio of the induced electromotive force and the electric field strength, which is therefore measured in units of length. To derive its expression from equation 6 a conversion to electric field has to be made through the relationship  $|\vec{E}| = c \cdot |\vec{B}|$ . The final expression for the effective height is shown in equation 7.

$$h_{eff} = \frac{\mathcal{E}}{E_0} = \frac{2\pi \cdot S_{eff} \cdot \cos(\alpha)}{\lambda} \quad (7)$$

Analyzing the expression it can be seen how for small magnetic loops it is intrinsically small on the VLF range as it has a dependence with the inverse of the wavelength. However, there are ways to compensate for this, by creating multi turn loops that maximize the effective area.

### 7.5.3 Radiation pattern of a small magnetic loop

In the previous section the expression that relates the electromotive force and the received field strength, shown in equation 7, was developed. This expression

can be used to compute the radiation pattern of our antenna.

Assuming that the received wave is vertically polarized, and the small loop antenna's surface vector is perpendicular to the floor surface vector, a dependence in azimuth can be observed. The source is the magnetic flux, which changes with the angle between the field and surface vectors. The normalized azimuth radiation pattern in natural units for a small loop with its surface vector pointing north is shown in figure 11a.

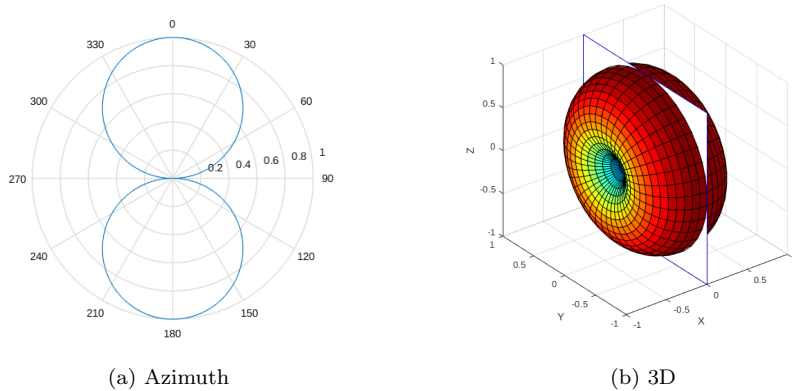


Figure 11: SML radiation pattern

In figure 11b the 3D radiation pattern is shown. In elevation the pattern is omnidirectional, which allows for the reception of the ionospheric modes with the same conditions. The maxima are located perpendicular to the loop surface vector, where maximum flux is achieved. Two nulls also appear where the flux is zero, which is an interesting property of this type of antennas. These zeros are often sharp and can be used to eliminate interference sources when orienting the antenna.

If the application requires an omnidirectional azimuth radiation pattern two loop antennas can be placed orthogonal to each other, with their surface vectors parallel to the floor surface vector. In this way the zeros of the radiation pattern will disappear as the zero from one antenna matches with the maxima from the other. This idea is shown in figure 12, where the radiation pattern contour of each loop is shown as a dotted line.

The radiation pattern of small magnetic loops resembles that of a dipole. In fact, they are often called magnetic dipoles as they couple to the magnetic field instead of the electric field while having the same radiation pattern.

Up to this point an antenna on free space has been considered when computing the radiation pattern. This is not the case on most situations, including our application, as it will be placed on ground.

Though the Numerical Electromagnetics Code (NEC) has limitations when simulating elements shorter than a hundredth of a wavelength, the antenna can be adapted to it while keeping it electrically small. Simulations were run using the 4nec2 software with different types of ground in terms of conductivity and electrical permittivity for a single turn small magnetic loop antenna. The results

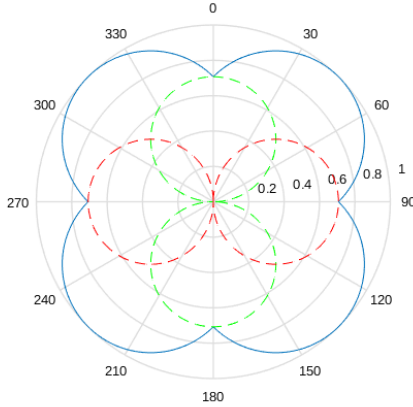


Figure 12: Radiation pattern for two orthogonal SML antennas

are shown in figure 13, where ideal and lossy ground cases are considered.

When over an ideal perfectly conductive ground the radiation pattern folds, maintaining its omni directional behavior in elevation above ground. However, when over non ideal ground, the result is a loss that can be modeled as an attenuation at low elevation angles. In the case of a transmitter at a distance of 2000 m, the angle at which the first mode is received is approximately  $2^\circ$ . This means that the ground wave and the first ionospheric modes will be attenuated. This effect cannot be avoided by raising the antenna above ground several meters or placing a conductive mesh below it as the scales are huge as determined by the wavelength.

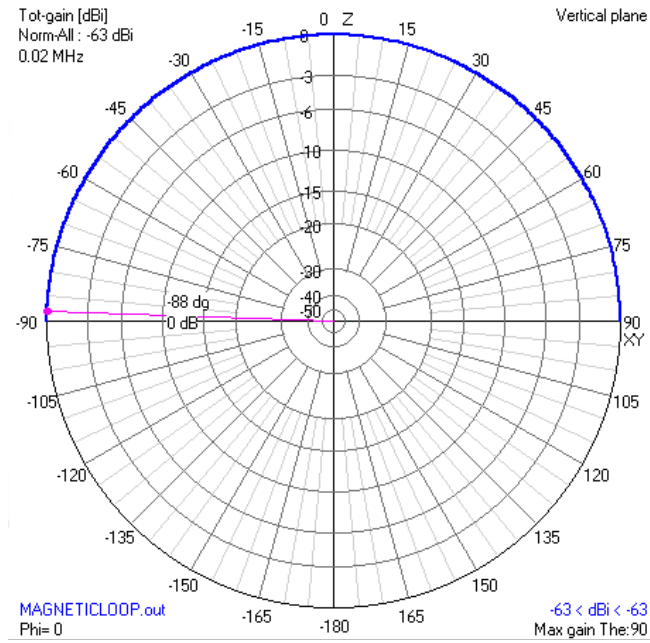
#### 7.5.4 Geometry of a small loop

Recalling section 7.5.2, where the expression for the effective height was developed, the dependence with the effective area is clear. For convenience it is shown again here.

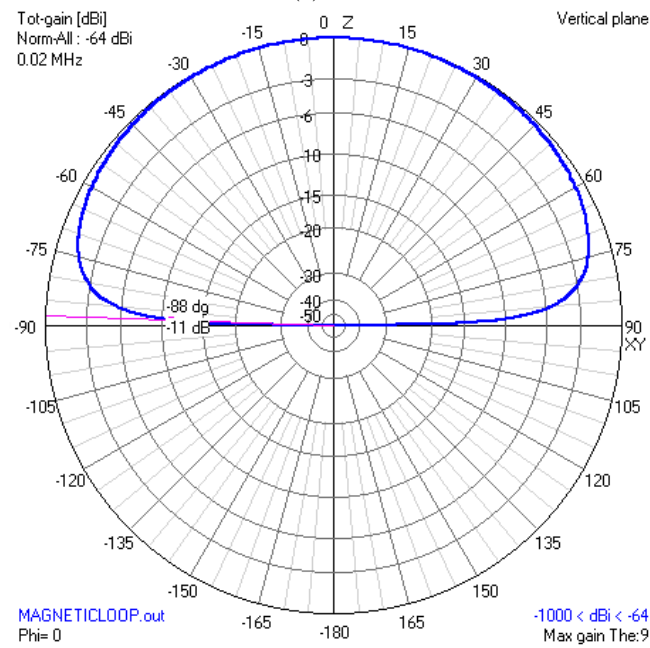
$$h_{eff} = \frac{\mathcal{E}}{E_0} = \frac{2\pi \cdot S_{eff} \cdot \cos(\alpha)}{\lambda}$$

$$S_{eff} = N \cdot S$$

As stated above, it is easy to notice that these types of antennas have intrinsically small effective heights for low frequencies given their dependence with the inverse of the wavelength. As the frequency is fixed it is necessary to maximize  $h_{eff}$  using other parameters. One option is by changing the orientation, but as it will be oriented with the aim of receiving with optimal conditions as many transmitters as possible,  $\alpha$  will be fixed. Therefore, the only way of increasing the sensitivity is by increasing the effective area.



(a) Ideal



(b) Lossy,  $\sigma = 10^{-4}$ ,  $\epsilon_r = 3$

Figure 13: Effect of ground on the radiation pattern

The limiting factor is the length of the wire used for the loop. It is then necessary to optimally wind the loop to get the highest effective area possible for a fixed length of wire.

The case for a single turn loop will first be considered. This allows to remove the number of turns,  $N$ , parameter from the equation. In this case, the area of the regular polygon enclosed by a fixed perimeter is given in equation 8, where  $n$  represents the number of sides of the polygon. The perimeter,  $P$ , represents the length of wire needed to enclose the figure. By computing for a range of values of  $n$ , as represented in figure 14, it is easy to see a trend.

$$S(n) = \frac{P^2}{4 \cdot n \cdot \tan\left(\frac{\pi}{n}\right)}, \quad n > 3 \quad (8)$$

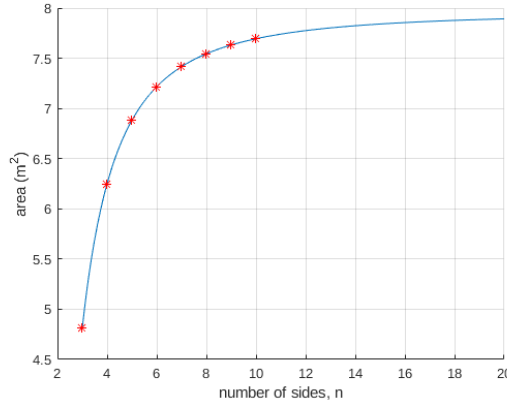


Figure 14: Area vs. number of sides for single turn loops with 10 m perimeter

This proves that regular polygons with few number of sides should be avoided, as they don't optimally use their perimeter. In fact, the best case is achieved when  $n \rightarrow \infty$ , which represents a circumference. As an example, the area enclosed by a circumference will be 65% greater than the area of an equilateral triangle given the same perimeter. Considering this dependence and the structural constraints that affect the construction of the antenna, an octagon will be used, as it only has a 6% area reduction over a circle while being easy to build.

Now the consequences of a multi loop coil will be analyzed. Given  $N$  as the number of turns and  $n$  as the number of sides of the regular polygon, the area can be computed following equation 9. In this case  $P_{tot}$  is the total length of wire needed to complete the specified turns, or in other words,  $P_{tot} = P \cdot N$ . Overall, the equation stays the same, though a dependence with  $N^{-1}$  can be observed. This produces a linear reduction of the effective area with the number of turns.

$$S(N) = \frac{P_{tot}^2}{N \cdot 4 \cdot n \cdot \tan\left(\frac{\pi}{n}\right)}, \quad n = 8, N > 0 \quad (9)$$

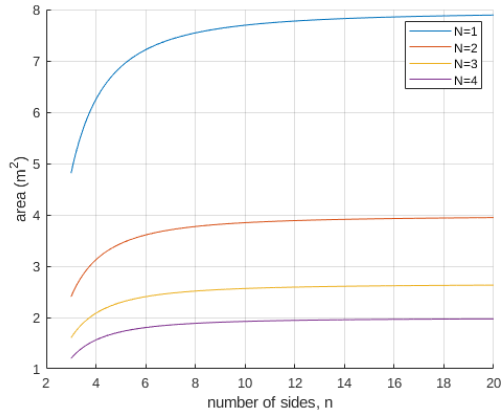


Figure 15: Area vs. number of sides for multi turn loops with 10 m total perimeter

Using a single loop provides the best results. However this loop may be too large to be constructed. In those cases a multi turn loop will be designed with the aim of increasing the effective area.

Searching for efficiency and easiness of construction, an octagon is a decent bet. For this specific case, a total of 250 m of wire will be used which, when arranged in an octagon of side length 44.9 cm, produces a total of 68 turns. This provides a total effective area of 69.22 m<sup>2</sup> which translates into an effective height of 29 mm at 20 kHz.

### 7.5.5 Electrical model of a small magnetic loop

As proven by Faraday's law of electromagnetic induction, a small magnetic loop inside a changing magnetic field will produce an electromotive force proportional to the rate of change of the magnetic field and other parameters. However, this doesn't mean that the electromotive force can be directly measured and sampled in the coil terminals. In reality, unavoidable phenomena as well as parasitic effects will influence the output signal, which the electrical model takes into account. In figure 16 the lumped element model for a SML with a non ideal voltage load is considered.

The components shown in figure 16 model the following effects:

- $V_1$ : Induced electromotive force due to Faraday's law of electromagnetic induction
- $R_A$ : Resistance of the antenna wire, radiation resistance, skin effect, ...
- $L_A$ : Inductance of the SML (coil)
- $C_A$ : Parasitic capacitances with the environment

- $C_L$ : Tuning capacitor
- $R_L$ : Preamplifier input impedance

It is easy to notice that the arrangement of these components composes a passive filter, that will indeed filter out certain frequencies. That's why it is necessary to analyze this model, as it is mandatory to check if the signal of interest is filtered by the non ideal characteristics of the antenna. However, this must be considered as a loose approximation, as the difficulty of theoretically modeling the system is elevated.

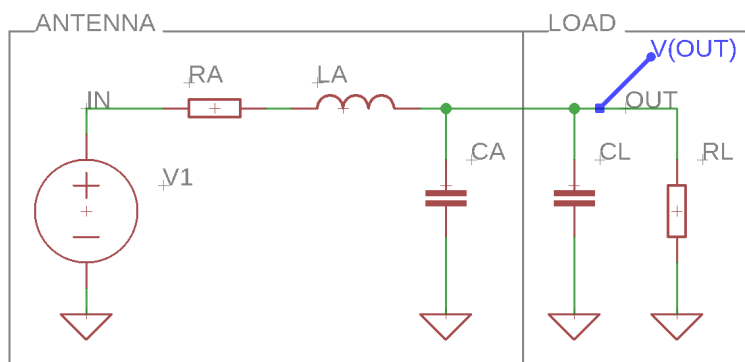


Figure 16: Electrical model of a small magnetic loop

First the resistive component will be analyzed,  $R_A$ , which is a mixture of several effects. Among them, these can be recognized:

- Wire resistance due to copper finite conductivity
- Radiation resistance
- Skin effect
- Proximity effect

Copper features a resistivity of  $1.68 \cdot 10^{-8} \Omega \cdot m$  at  $20^\circ\text{C}$ . Without taking into account temperature dependence, the wire resistance from copper's non zero resistivity is given by the next expression, where  $\rho$  is the resistivity,  $L$  the conductor length and  $A$  the cross sectional area.

$$R = \frac{\rho L}{A}$$

This component is the one that will produce thermal noise and will be present at all frequencies. Furthermore, it is the only one that can be measured using a multimeter, as it exists at DC.

For 250 m of 23 American wire gauge (AWG) tinned copper wire, the direct current (DC) resistance is  $16.6 \Omega$ .



The radiation resistance represents the effect of energy leaving the antenna as radiating fields. For a SML is usually very small [13], so it can be neglected.

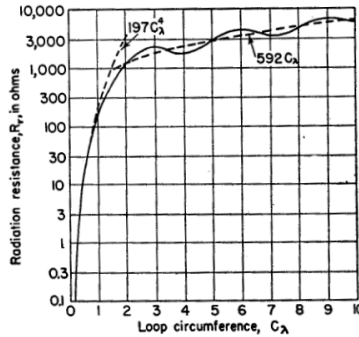


Figure 17: Loop radiation resistance vs. its perimeter in  $\lambda$  as given by Krauss

In this case the antenna perimeter is below 10% of a wavelength. For this case the radiation resistance quickly decreases with the wavelength to antenna perimeter ratio. For electrically small antennas, the radiation resistance can be approximated with the following expression:

$$R_{rad} = 197C_{\lambda}^4$$

As proven by Krauss [13] in figure 17, the value will be negligible.

The so called skin effect represents the fact that alternating current (AC) current does not penetrate the whole conductor with an uniform current distribution, but its density decreases exponentially the further away the surface is. For frequencies much lower than  $\frac{1}{\rho\epsilon}$ , where  $\rho$  is the resistivity of the material and  $\epsilon$  its permittivity, the the skin depth is given by the following equation, where  $\mu$  is the magnetic permeability of the material and  $\omega$  the angular frequency of the flowing AC current.

$$\delta = \sqrt{\frac{2\rho}{\omega\mu}}$$

This effect produces an increase of the resistance which depends on the frequency as shown in figure 18. It can be seen that for frequencies in the kilohertz range is almost negligible. Solving for this case, at 20 kHz, the resistance increases by 0.64  $\Omega$  up to 17.1  $\Omega$ .

The last effect that adds to the total resistance,  $R_A$ , is the proximity effect. It is produced when at least two conductors carrying AC currents are placed in close proximity. Due to the magnetic fields produced by the flowing current, a force will be exerted over the moving charges of the other conductors, constraining those charges to smaller regions of the conductor. This results in an increase of the AC resistance, as the current distribution is not uniform across the conductor's cross section. Single turn loops are obviously not affected by the proximity effect, and it is prevalent in transmitting loops due to the high

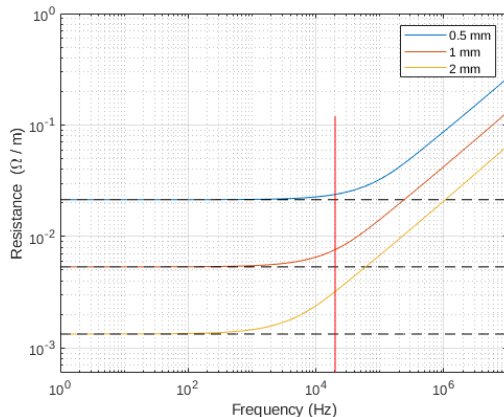


Figure 18: AC resistance of a wire with different radii

current that flows through them. In the case of an open circuited receiving loop it could be argued that as no current flows through it, it won't be affected. However, even when open circuited, a current will flow.

The only way charges can accumulate on the leads of a loop is by moving through the conductor. In presence of a sinusoidally changing magnetic field the charges will move at a frequency equal to the changing field. This means that a receiving multi turn loop will suffer from proximity effect to some extent, but not nearly as much as a transmitting one. Calculating this component is difficult, often unreliable due to the high amount of variables involved, and it is therefore out of the scope of this project.

The next effect to consider is the inductance, which measures the opposition that will be produced against changes in current. All the expressions and procedures for computing the inductance of the coil can be found in Grover's Inductance Calculations book [14]. There, he presents a collection of methods and formulas that will suit our needs. However, as multi-turn loops are not considered, a way of describing a coil as a combination of windings is needed.

The inductance of a coil can be described as a sum of the self inductances of each winding plus the summation of the mutual inductances between them. An easier way of looking at this to imagine several single loops connected in series. As in our case, the windings are commutatively coupled the mutual inductance adds, and not subtracts. This idea is described in equation 10

$$L = \sum_{i=1}^N L_i + \sum_{j=1, k=1}^{N, N} M_{jk} ; j \neq k \quad (10)$$

Bashenoff approximation for a single turn polygonal loop is shown in equation 11, where  $\rho$  is the material resistivity,  $\mu$  the relative permeability of the material,  $l$  the perimeter of the figure,  $S$  the enclosed area and  $\phi$  a value dependent of the ratio  $\frac{l}{\sqrt{S}}$ .

$$L = 0.002 \cdot l \left[ \log_e \frac{2l}{\rho} - \left( 2 \log_e \frac{l}{\sqrt{S}} + \phi \right) + \frac{\mu}{4} \right] \quad (11)$$

Solving for one octagonal turn of 45.9 cm side length wined with 23 AWG copper wire a total of 5.76  $\mu\text{H}$  per turn are obtained. Extending to 68 turns, the total self inductance of the windings is 392.02  $\mu\text{H}$ .

As for the mutual inductance there is no easy way of computing it. For a coil, the mutual inductance of adjacent windings can be considered to be equal, but considering all the combinations of windings is insane. To account for the effect of each winding over the rest, a total of  ${}^{68}P_2 = 4556$  iterations are needed.

In our case, due to the structure used, as it is intended to sit outside and be easily movable, not much attention will be payed into maintaining a specific order when winding the coil. Therefore, the calculation of the total mutual inductances of the coil presented here will be inaccurate, and should only be considered as a far approximation.

Grover gives a method for an arbitrary number of sides following equation 12, but discourages its use when the polygons are close together due to inaccuracies in the interpolation of the F value.  $N$  is the number of sides of the polygon,  $s$  the side length of the polygons and  $d$  the distance between their planes. Values for  $f$  and  $F$  can be found in tables in Grover's book.

$$M = \frac{Ns}{2\pi} fF \quad (12)$$

As in our case the polygons may even be coplanar, other approximations have to be considered. Specific equations are given for coaxial hexagons, squares and equilateral triangles, but not for octagons. However, as it is not a critic value, an approximation will be enough. The hexagon series formula shown in equation 13 will be used.

$$M_{hex} = 0.012s \left[ \log_e \frac{s}{d} - 0.15152 + 0.3954 \frac{d}{s} + 0.1160 \frac{d^2}{s^2} - 0.052 \frac{d^4}{s^4} + \dots \right] \quad (13)$$

The calculations will be done as if the octagons were hexagons of the same perimeter, as this makes them equivalent figures. This means that the hexagon area will be slightly smaller than the octagon's. This will compensate the fact that the equation is designed for an hexagon to some extent, as higher N polygons have higher mutual inductances for the same perimeter.

Solving for 68 turns of 0.8 cm spaced windings of 45.9 cm side length we obtain a total mutual inductance off 1999.3  $\mu\text{H}$  that when added to the self inductance, following equation 10, gives 2391.3  $\mu\text{H}$ .

As with proximity effect, parasitic capacitances due to the arrangement of the conductor and due to the coupling with the environment are difficult to predict as they not only depend on the shape of the coil but also on how and where the coil is placed. However, these should be small. As a reasonable approximation these can be considered in the hundreds of pico farads range

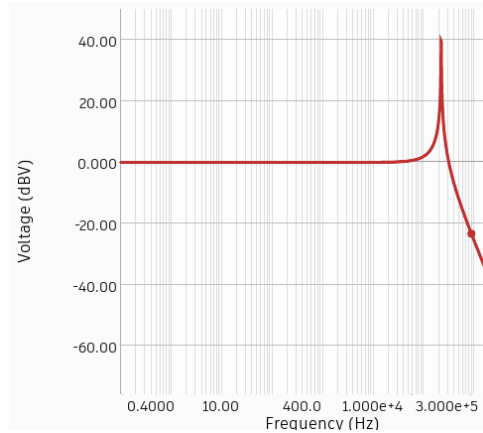


Figure 19: Simulation of the model with the theoretical approximation

[15], 200 pF will be used for our case.

The loading effect of the preamplifier block, modeled by  $R_L$ , will not be analyzed, as it is easy to obtain a reasonably high input impedance, and therefore, its loading effect on the antenna is negligible.

The simulations shown in figure 19 show the low pass filter behavior of the antenna. However, the 3dB cut off frequency is more than a decade away from our frequencies of interest. Of course, this is not accurate, but gives an idea of what to expect. In theory then, at 20kHz, no additional attenuation will be present due to the effects of the antenna.

### 7.5.6 Maximizing the SML SNIR

The Signal to Noise Ratio (SNR) is a relationship between the levels of signal and noise. Often this measurement also considers interferences (SNIR) from other systems that use the same band polluting it. In the case of VLF both have significant impact, though the latter can sometimes be avoided.

In this case, as there is no demodulation, talking about bit error rates (BER) is irrelevant. Therefore, this analysis will focus on defining the noise and interference sources which degrade the SNIR and how to maximize it. The general expression for SNIR is shown in equation 14, where  $S$  represents the logarithmic signal level and  $n$  and  $i$  the natural level of noise and interferences.

$$SINR = S - 10\log(n + i) \quad (14)$$

Noise sources can be classified as internal or external depending on the source. Internal sources are in the system itself, while external ones are in the environment. The ITU gives in the P.372 recommendation [16] a list of procedures and graphs which aim to guide the design of systems where noise must be considered.

While there are several internal noise sources, the only one that will be considered due to it being remotely significant is thermal noise. This type of noise is produced by the agitation of charged particles (electrons) on a conductor due to their non zero thermal energy. It can be characterized by just one parameter, the noise spectral density, as it presents a white spectrum. It is this value the one that determines the thermal noise level in the system. Its RMS voltage spectral density is given by the expression shown in equation 7.5.6, where  $K$  is the Boltzmann constant.

$$V_{rms} = \sqrt{4KTR}$$

From this expression it can be noted that the physical temperature ( $T$ ) of the wire in the antenna coil, as well as its resistance ( $R$ ), will have an impact. This is of course fixed for the antenna, as long as temperature remains constant.

Ways of increasing the signal while maintaining a constant level of thermal noise have already been discussed in section 7.5.4, as the resistance is linearly dependent on the total perimeter of the coil. Therefore any design that decreases the total perimeter while keeping a constant effective area will decrease the thermal noise level.

In regards to external sources, the ones with greater impact in the VLF range as given by the ITU are:

- Atmospheric noise
- Man made noise or industrial noise
- Galactic noise

These are shown in figure 20, where the noise temperature is graphed for a range of frequencies on different conditions. It can be noticed that galactic noise only affects the megahertz range. The rest however, have great impact at kilohertz frequencies, and are the main sources of noise of our system.

In the VLF range, the main source of atmospheric noise are lightnings [17]. These produce emissions that can propagate through the Earth-ionosphere waveguide, surrounding the whole globe and affecting receivers even if no storms are nearby. The result is a fairly constant level noise background and, due to its global effect, cannot be avoided. Individual events will most likely not be detected by this system due to the rather high spectral sampling period (5 s) and averaging taking place during logging. Specific terminology has been developed to distinguish between different types of lightning emissions, which are: sferics, tweeks, whistlers and chorus.

Man made noise is produced by human activities and industrial processes. It is more significant in industrialized and urban areas and can be reduced to some extent by placing the whole system away from them. However, this is usually not feasible as for convenience the antenna will preferably be in a near and easy to access location.

The last degradation of the SINR comes from interferences. These are much more local as they are produced by nearby devices and appliances which radiate at kilohertz frequencies and, unfortunately, are extremely common and powerful

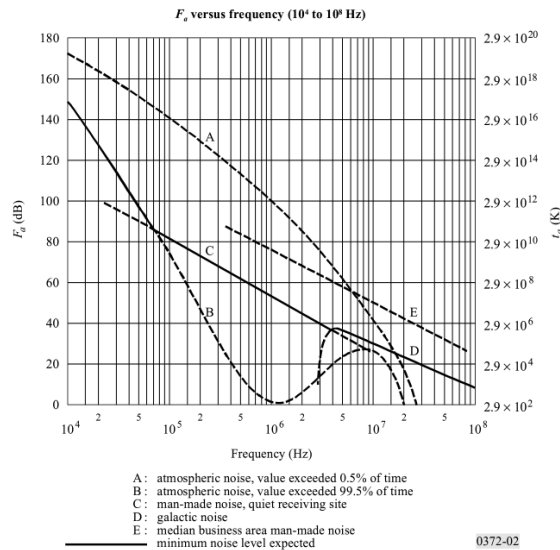


Figure 20: Noise temperature vs. frequency graph given by the ITU on P.372

enough to be an issue. The main difference with external noise is that they can be avoided by carefully selecting the antenna location and keeping at a reasonable distance devices and appliances. For example, an office building will offer a worse environment than a gardening storage booth away from buildings.

Common sources of interferences are switching power supplies, which nowadays are used everywhere due to their high efficiency and small volume. These operate at frequencies of around 20 kHz and are usually not well shielded. Motors in general, such as those used in ventilation systems are also an issue. However the worst type of them are stepper motors, as they need to be driven by high frequency high intensity pulsating currents. These are commonly found in printers and scanners.

One interesting case are loudspeakers from audio systems, which produce interferences as audio falls inside our band of interest. Even if sound is a mechanical wave, their working principle involves alternating current flowing through a coil, which will radiate alternating magnetic fields.

Finally, one of the most significant and constant sources of interference are power lines. These induce 50/60 Hz tones, but as these are out of the band of interest, they are usually not a problem. However, when designing the amplifier special care must be taken to avoid desensitization or saturation either in the amplifier itself or the sound card.

## 7.6 Physical build

The structure of the antenna must be able to withstand adverse weather conditions in case it is placed outside. Metallic materials are obviously discarded, as they would form a loop by themselves and, while plastic fits our needs, it is

sometimes difficult to build a structure that can support itself without deformations. The obvious choice then is wood, but as not all woods are made equal, it was necessary to choose one that could withstand outdoor conditions.

From the wide range of woods available, Iroko wood was chosen to build the structure. This type of wood is commonly used in boats and doors and requires minimum maintenance. Several beams were given to a carpenter, with the instructions to build an octagon with its support structure. The resulting masterpiece is shown in figure 21. It has to be noted that no screws or nails were used to join the different pieces of wood, just wood joinery techniques.

Once the structure is complete, the loop can be wound. Using 23 AWG solid core copper wire a total of 68 turns were made. These all fit in a groove carved on the wood in the side of the loop, shown in figure 22. Finally, once the winding is finished, the exceeding length of the wires must be twisted until they are soldered to the coaxial cable. This improves interference rejection as the fields cancel each other. This principle is the same used in the telephone twisted pair.

## 7.7 Circuitry

To sample the signal coming out of the antenna, a common personal computer (PC) sound card will be used. These usually come in a range of sampling rates, from the typical 44 kHz to the high end 192 kHz. Additionally, this solves many problems, as in a computer we find all that is needed: storage media, sampling device with an easy to use interface, enough computing power to solve a fast Fourier transform (FFT) real time and network capabilities to send the logs to a SFTP server.

Due to the Nyquist-Shannon Sampling Theorem [18], to obtain the complete information of a band limited signal it must be sampled at least at double its bandwidth. Furthermore, the anti-aliasing filter built at the input stage of the sound card will remove any signal above the set frequencies. By using a 44 kHz sound card frequencies up to 22 kHz can be sampled.

Though this setup alone could ideally work, the signal levels coming out of the loop are so weak that they need to be boosted. As the antenna will be placed far away from the computer, the signal will be transmitted over long wires. This makes amplification necessary to give the signal immunity to interferences along the path. For this purpose an active filter will be designed in order to filter out unwanted frequencies as well as to provide decent amplification.

In figure 23, the simplified block diagram for the complete system is shown, which consists on an amplifier with noise figure  $F_2$  and gain  $G_2$ , a filter with attenuation  $L_3$ , and the cables that carry the signal from the antenna to the amplifier and to the computer modeled as passive purely resistive attenuators with attenuation  $L_1$  and  $L_4$  respectively. The receiving chain can be characterized with its total gain and the noise factor. Though the total gain is determined by the gain of the filter and the attenuation of the cables, the noise factor can be optimized with the arrangement of the elements.

The noise factor ( $f$ ) is a representation of the deterioration of the SNR along the system. As given by Friis formula [19], shown in equation 15, having a high gain and low noise factor amplifier as the first element of the chain reduces the total noise factor as the rest of the terms are divided by that first element gain.



Figure 21: Antenna structure





Figure 22: Coil windings

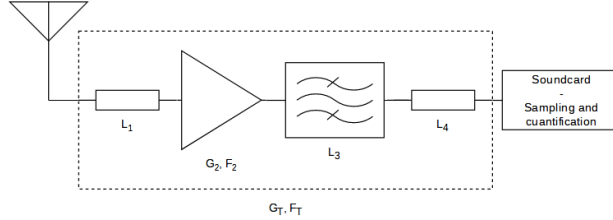


Figure 23: Simplified block diagram of the complete system

For this reason the amplifier will sit right next to the antenna, while the long transmission cables will be connected to its output. That way the attenuation  $L_1$  will decrease in favor of  $L_4$ , improving the overall noise factor of the system.

$$f_T = f_1 + \frac{f_2 - 1}{g_1} + \frac{f_3 - 1}{g_1 g_2} + \frac{f_4 - 1}{g_1 g_2 g_3} + \dots \quad (15)$$

Having the amplifier placed next to the antenna implies that power must be sent to it in some way. Mains voltage should be avoided, as it would require outdoor weatherproof cables and outdoor plugs with the added security risks. One option is sending the supply current through the returning signal wires. This concept is called phantom power and is typically used in television antenna systems. However, when working in the VLF range the filters require huge inductors and capacitors to provide decent filtering at such low frequencies, which makes using this technique unfeasible.

Instead of sending DC over a cable all the way up to the amplifier, it has been decided to send the AC output of a transformer which also suits the selected power supply topology as it is shown in section 7.7.2. Finally, the distribution of the equipment is represented in figure 24.

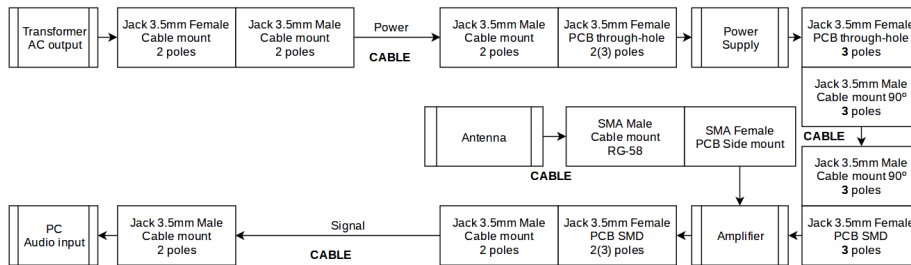


Figure 24: Connection diagram

The connections of the whole system are made up of 3.5 mm audio jacks as they are small and easy to find. The downside is that care must be taken when making the connections, as they all look the same. Mistakes can be avoided by properly labeling the connectors at each end.

### 7.7.1 Preamplifier

This block aims to adapt the characteristics of the signal coming out of the antenna so that it can be sent through a long enough cable and sampled by the computer's sound card. To achieve this, amplification is required, which will be supplemented with filtering. A design around operational amplifiers is proposed, as it solves lots of design considerations. Some of them are: the biasing is easily solved with the supply pins, it is easy to set up active filter configurations and they have high-enough gain bandwidth (GBW) products to allow for high gain designs.

By design the antenna gives its output as a voltage source, which means that it should be loaded with an infinite impedance or at least, reasonably high. As a consequence, the preamplifier input impedance must be high enough to minimize the detrimental loading effects on the signal as its connection to the antenna forms a voltage divider. Achieving this is easy as operational amplifiers nowadays have extremely high input impedances, commonly in the range of a few mega ohms and above.

Dividing the amplifier in two stages provides some benefits. First, a bandpass filter can be built by combining a high pass response and a low pass response in cascade, and second, as the gain is shared, designs with greater bandwidth can be built.

For the first stage, represented by X1 to X4 in the schematic shown in page 50 (section 8), an instrumentation amplifier will be used. It is an arrangement of three operational amplifiers which provide a differential input with a referenced output. As a consequence, the output will be directly proportional to the difference between the two inputs which in this case is the electromotive force induced in the coil. In addition, it also offers buffered inputs by design, which provide extremely high input impedances. To save space, as well as to simplify the whole board, an integrated circuit already containing the arrangement of an instrumentation amplifier will be used. The one selected for this project is the INA128 by Texas Instruments.

By creating a single pole low pass filter with an operational amplifier the INA128 can behave as a high pass filter with the gain specified by the  $R_1$  resistor and the pole set at  $\omega = \frac{1}{R_2 C_1}$ . As it is not only the module of the transfer function that matters, but also its phase, it is not possible to develop higher order filters as feedback network. The operational amplifier is needed as the reference pin must be driven by a low impedance source. This arrangement is named AC-coupled instrumentation amplifier, as given in the INA128 datasheet.

The transfer function for the INA128 with the feedback network is shown in equation 16 where the components are labeled according to the schematic.

$$H_1(s) = - \left( 1 + \frac{50 \cdot 10^3}{R_1} \right) \cdot \frac{s}{s + \frac{1}{R_2 C_1}} \quad (16)$$

The second stage, formed by X5, provides a first order low pass response. Though it would have been possible to design a higher order filter like the Sallen Key configuration, a first order filter was decided to be the best option as it allows for gain tuning using a potentiometer without modifying the cut off frequencies. The transfer function for this stage is shown in equation 17.

$$H_2(s) = -\frac{R_4}{R_3} \cdot \frac{1}{1 + sR_4C_2} \quad (17)$$

Finally, as the combination of these two filter blocks in a cascade arrangement creates a total transfer function equal to the multiplication, the expression for the complete system can be derived. This is shown in equation 18 and represented in figure 25 as a function of frequency.

$$H(s) = \frac{R_4}{R_3} \cdot \left(1 + \frac{50 \cdot 10^3}{R_1}\right) \cdot \frac{s}{\left(s + \frac{1}{R_2C_1}\right) \cdot (1 + sR_4C_2)} \quad (18)$$

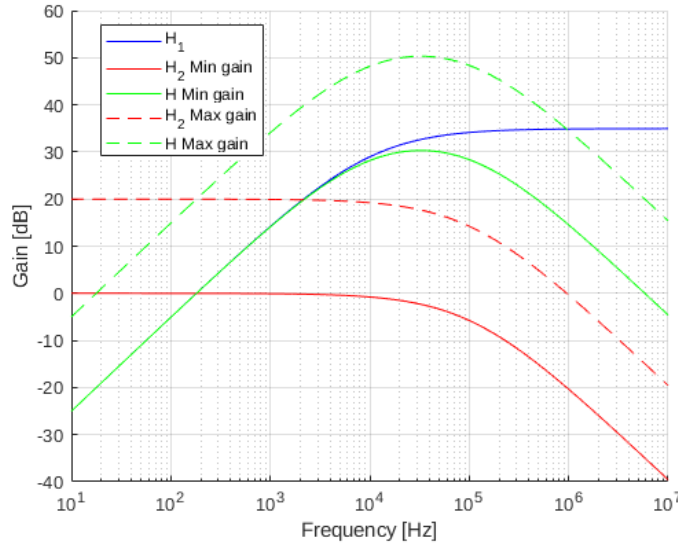


Figure 25: Transfer function of the filter

Having an amplifier with variable gain is important as the received field intensity cannot be calculated. This allows for the gain to be adjusted on site to avoid saturation. Though the computed theoretical gain is between 35 dB and 55 dB in practice should be smaller as the poles are close together, which produces a reduction in the total gain.

Though it would have been easier to adjust the gain using  $R_1$ , it has been decided to fix the gain of the first stage. This tries to avoid degradation on the signal as at that point is at its weakest.

As a final consideration it is necessary to stress the importance of  $R_5$  and  $R_6$  resistors as, due to the design, bias currents don't have a path to ground through the loop. Therefore, it is mandatory to provide one using additional components.

The complete design schematic and printed circuit board (PCB) design are

available in section 8. From them, the circuit was built using a milling machine on FR4 substrate. The result is shown in figure 26, with dimensions of only 37x26 mm.

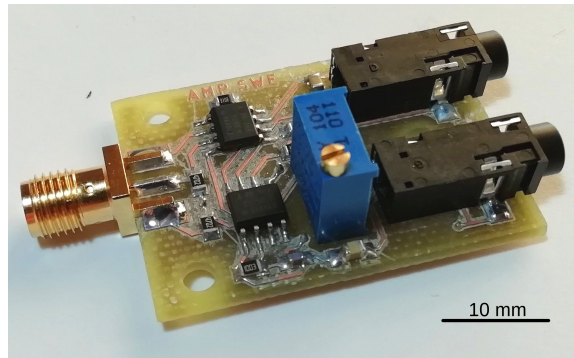


Figure 26: Amplifier PCB

During testing the total current consumption was found to fall around 20 mA.

### 7.7.2 Power supply

As the signals of interest have frequencies of about 15 kHz to a few tens of kilo hertz, special care must be taken when designing the power supply as any switching noise will degrade our signal. For this reason, switching power supplies must be avoided, as their switching frequencies are right in the band of interest. The only viable option is then a linear power supply.

This kind of supplies have several advantages as they are very simple to design and build, have high ripple rejection and lack any switching noise due to its working nature. However they are highly inefficient as they dissipate the extra power as heat. Given that our application won't require anything more than a few milli amperes, this shouldn't be a problem.

The topology of this supplies, which is shown in figure 27, is composed of four easily distinguishable parts: the transformer, bridge rectifier, filter and linear regulator. First the 240 volt AC is fed into the transformer, which outputs a lower AC voltage. Then the bridge rectifier converts the AC input to a only positive/negative but non constant voltage which is then filtered by the (usually big) filter capacitor. The voltage regulator helps with ripple rejection and provides a constant voltage output independent of the demanded current.

In this case the transformer sits next to the computer, while the rest of the supply is at the antenna location. This allows to send the fused lower voltage AC through a cable. The transformer should give an output of at least 16 V effective for it to be able to power the preamplifier as  $\pm 5$  V DC are required.

Even if the current demand for the load will be small, a full bridge rectifier will be used as it produces less ripple than a half bridge under the same load and with the same filtering capacitor. Furthermore, capacitors in parallel to each

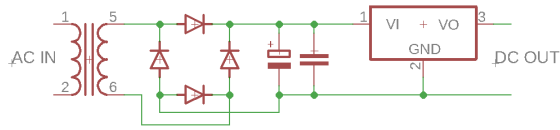


Figure 27: Linear power supply topology

of the diodes will be placed to reduce the high-frequency components produced by the abrupt change in the reverse recovery current of the diodes, although it should be unnecessary.

A typical choice for a positive voltage linear regulator is the famous LM317. In its "L" version it can provide up to 100 mA in a TO-92 package, which is enough for our purposes. It also allows for a variable output, which can be fixed through two resistors following the expression shown in equation 19.

$$V_{out} = 1.25 \left( 1 + \frac{R2}{R1} \right) + I_{adj} R2 \quad (19)$$

Finally, as this voltage is floating, a way of dividing it in two is required to build the symmetric power supply. This can be easily achieved with an operational amplifier in buffer configuration and a resistive divider at its input. These two resistors should be equal. Values between 4 k $\Omega$  and 100 k $\Omega$  are acceptable.

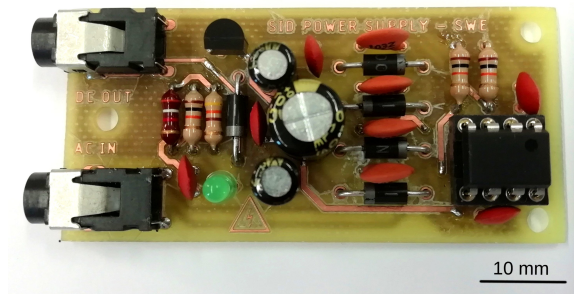


Figure 28: Power supply PCB

Though this design is provided for low noise operation it is definitely overkill. If replicated, it is left to discretion of who tries it the the use of all the additional components. The complete schematic and PCB design can be found in section 8.

Again, using a milling machine and FR4 substrate, the board was built. The result is shown in figure 28, which has dimensions of 60x30 mm.

## 7.8 Measurements

Once the system was all set up, a computer was configured with EricGibert software, SuperSID, available at GitHub ([github.com/ericgibert/supersid](https://github.com/ericgibert/supersid)). This software controls all the sampling and logging tasks that are required for the selected frequencies, and outputs the raw data to a file. Data were taken at 5 seconds sampling period and then filtered by a moving average of 13 coefficients.

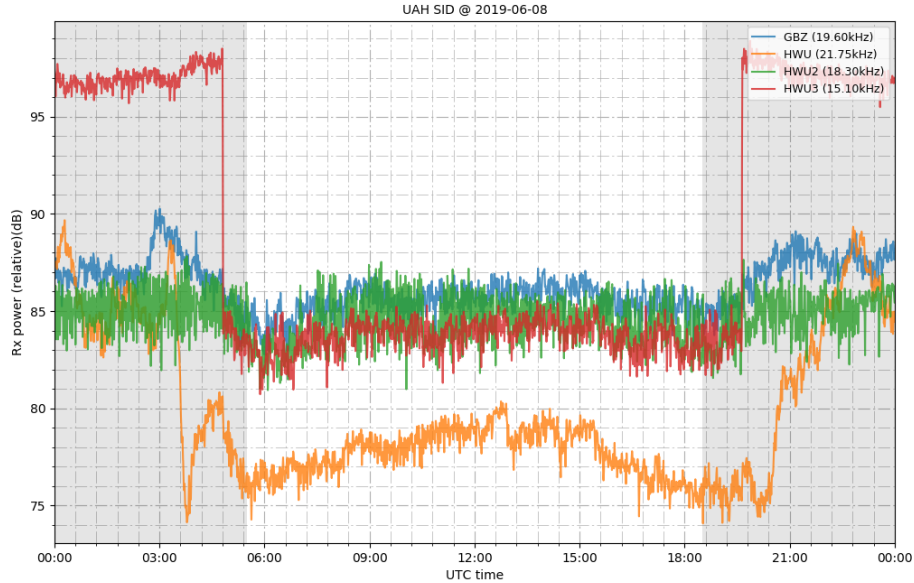


Figure 29: Measurements obtained during the 8<sup>th</sup> of June

It was then left for several days to measure the daily variations. After that, using `sid_plot`, the data were plotted. This is a python script developed for this project based on EricGibert's `supersid_plot` which allows to plot the data while including additional functionality. It is available at GitHub ([github.com/AlbertoGM97/sid\\_plot](https://github.com/AlbertoGM97/sid_plot)) as well. The output plot for one of the days is shown in figure 29.

The featured stations are GQD, as GBZ, from Anthorn (United Kingdom) and the HWUx series from Rosnay (France). GQD is one of the most notorious transmitters among VLF logging stations as it rarely goes on maintenance and can be easily received from Europe.

All the data were obtained from the second floor of the Polytechnic School, so it is not surprising the amount of noise that can be seen. Even so, the day-night cycle can be distinguished clearly on three of the logged frequencies.

Both, GBZ and HWU, show the typical curves for the day, with a higher signal level during the night due to the disappearance of the D layer and the more constant level with a slight curvature during the day. This curvature is due to the change in the incidence angle of solar radiation. It is therefore maximum at local noon. In the case of HWU2, even if the day-night transitions

can barely be distinguished it is mostly noise. This suggest that this transmitter was turned off during the time of recording, which was confirmed once it was turned back on during the 11<sup>th</sup> of June (see figure 30).

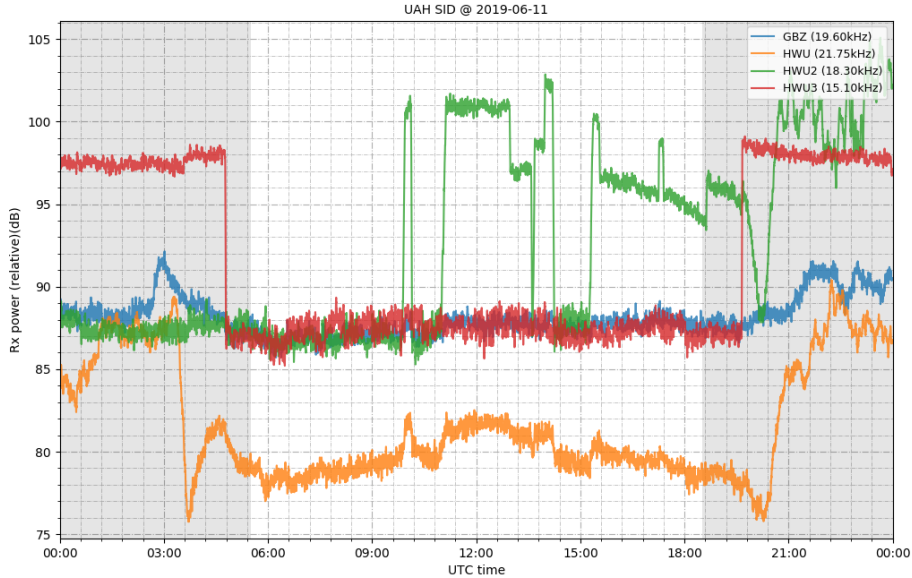


Figure 30: Measurements obtained during the 11<sup>th</sup> of June

## 7.9 Data processing

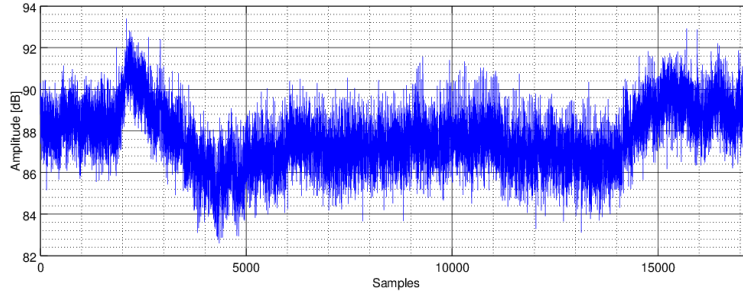
The data presented in section 7.8 shows a fairly high level of noise even when filtered with a 13 sample moving average. However, improvements can be made by looking closely at it. It is the purpose of this section to analyze the data and find ways to reduce the root mean square (RMS) noise value while keeping as much of the original information as possible.

The raw dump for GBZ captured on the 8<sup>th</sup> of June is graphed in figure 31a. From it, using a flat region, the RMS noise level was computed as 1.016 dB. In figure 31b the power spectral density is plotted.

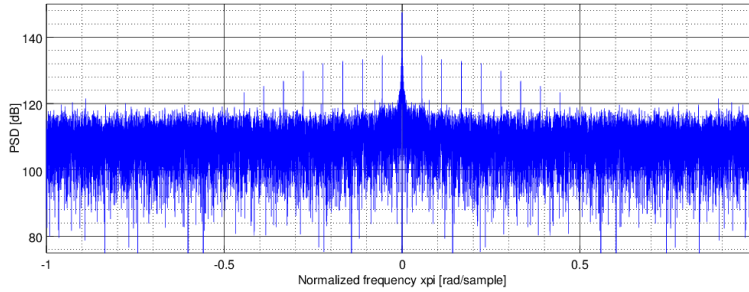
When looking at how the power is distributed along the spectrum several spectral components can be distinguished. These do not belong to the variations of the signal produced by the changes in the ionosphere, but are produced by a nearby device, which periodically emits interferences in the VLF band. The effect of a train of periodic pulses in the time domain is a sinc function in the frequency domain.

A way of filtering these spectral components is needed, but by filtering them information will be lost. Fortunately almost all of the information related to changes in the ionosphere is located in the band below  $0.04\pi$  rad, which corresponds to frequencies below 25.1 mHz. In figure 32, a system capable of isolating the central frequencies is proposed.





(a) Time domain



(b) Frequency domain

Figure 31: GBZ raw data captured on the 8<sup>th</sup> of June



Figure 32: Digital processing system

This system approaches the problem in three phases with the aim of preserving the band of interest, which is approximately below  $0.04\pi$  rad. By using these three stages the requirements of the filters are reduced, which translates into fewer coefficients for their impulse response. Furthermore, down sampling also allows to reduce the total output file size while keeping all the information from that central band. Of course, the raw dumps must be stored as they contain more information than the filtered logs and can also serve to precisely determine the timing of flare events due to the higher number of samples.

FIR filters will be designed following the window method as they are inherently stable. With this method the impulse response is computed with the windowing of the impulse response of an ideal filter, as shown in equation 20, where  $\Omega_c$  is the 3 dB cut off frequency and  $M$  the order of the filter. This process is illustrated in figure 33 which shows the window,  $w[n]$ , over the ideal filter impulse response. Zero-phase filtering techniques will be used, which try to compensate the phase of the filter and present an amplitude response squared

to the designed filter. As a consequence of this process, the effective total number of coefficients is doubled. The impulse response coefficients for both filters can be found within the code provided in section 7.9.1.

$$h_d[n] = \frac{\sin(\Omega_c \cdot n)}{\pi \cdot n} \cdot w \left[ n + \frac{M}{2} \right] \quad (20)$$

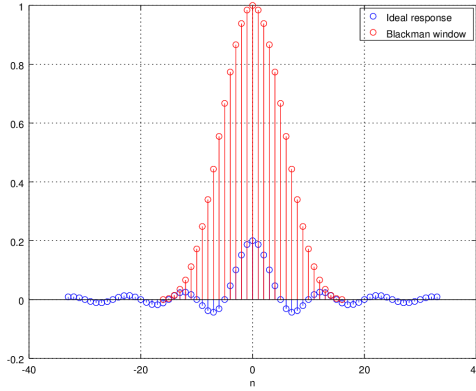


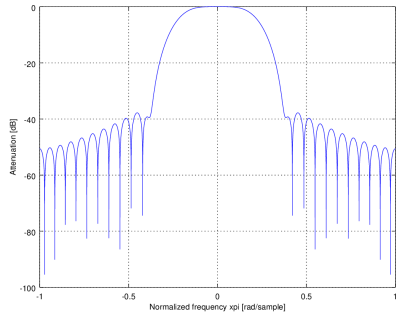
Figure 33: FIR impulse response by the window method

The first filter ( $H_1(\Omega)$ ) aims to remove the spectral components above  $\frac{\pi}{5}$  rad. The transfer function is shown in figure 34a. This filter, with 33 coefficients ( $M = 32$ ), uses a Blackman window [20]. The reason for this is that as the bandpass region is broader than the information that will be kept, the slower transition is not a problem. In addition, this window provides better stop band levels than Hanning and Hamming windows [20]. Once filtered, the data's power spectral density is shown in figure 35a.

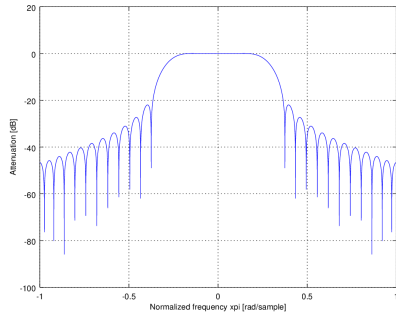
Once the higher frequencies have been filtered, the data can be down sampled to spread the spectrum. A down sampling of index  $M = 6$  has been chosen as even if it produces significant aliasing on the outermost part of the spectrum, the inner band is kept with minimum alterations. This step reduces the constraints of the last filter,  $H_2(\Omega)$ . The power spectral density of the signal after down sampling is shown in figure 35b.

Finally, the last filter is designed to filter out frequencies above  $0.27\pi$  rad, as the band of interest has widened by a factor 6. Again, 33 coefficients are used ( $M = 32$ ), but now with a Hanning window, as it provides sharper transitions from pass band to stop band for the same number of coefficients [20].

After this last filter, all the interfering spectral components have been removed. Now, the RMS noise value has been reduced to 0.2704 dB. The result is shown in figure 36.

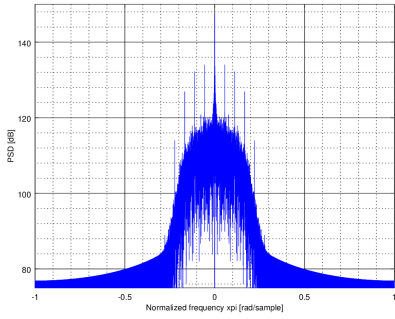


(a)  $H_1(\Omega)$

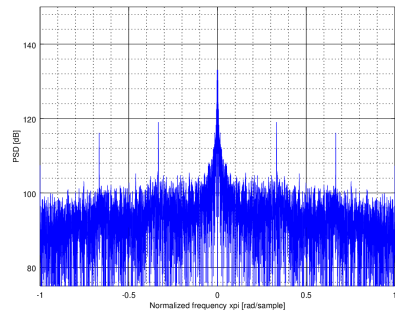


(b)  $H_2(\Omega)$

Figure 34: Transfer functions of the digital filters

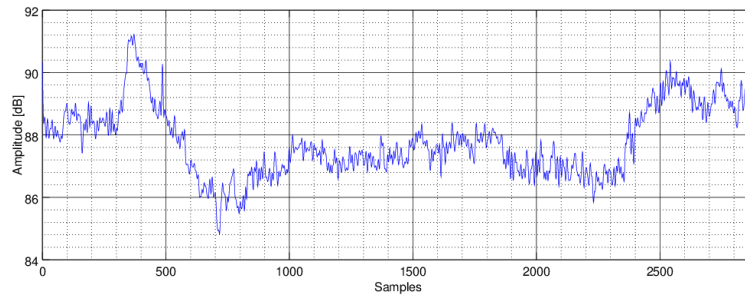


(a)  $X_1(\Omega)$

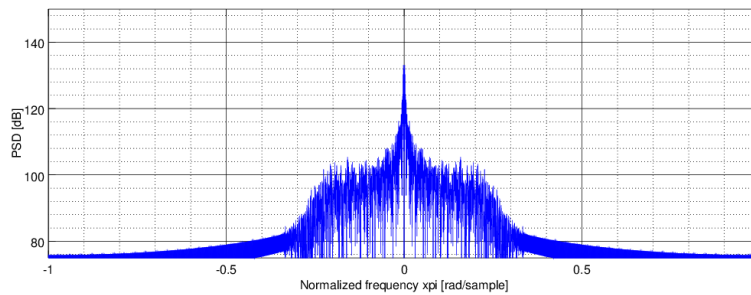


(b)  $X_2(\Omega)$

Figure 35: Intermediate steps



(a) Time domain



(b) Frequency domain

Figure 36: Processed data

### 7.9.1 Plotter script

A script to produce the output graphs featured in figure 29 and 37 has been developed. It incorporates the digital signal processing system designed in this section to filter out noise, as well as other options. It is open source and is publicly available at GitHub ([github.com/AlbertoGM97/sid\\_plot](https://github.com/AlbertoGM97/sid_plot)).

```

1
2 *****
3 # Based on supersid_plot.py from
4 # https://github.com/ericgibert/supersid
5 #
6 # Adaptation by Alberto Garcia Merino
7 # https://github.com/AlbertoGM97/sid_plot
8 *****
9
10
11 import argparse, csv, time
12 from datetime import datetime, timezone, timedelta
13 import numpy as np
14 from scipy import signal
15 import matplotlib as mpl
16 from matplotlib import dates

```

```

17 import urllib
18
19 import sys
20
21 parser = argparse.ArgumentParser(description = 'usage:
python3 sid_plot.py file1.csv file2.csv [Options]')
22 parser.add_argument('-f', '--filter', dest = 'filter',
help='Filter with moving avg',action='store_true')
23 parser.add_argument('-c', '--custom', dest = 'custom',
help='Custom two-phase filter',action='store_true')
24 parser.add_argument('-l', '--logy', dest = 'do_log', help =
'Use logarithmic scale on Y axis', action = '
store_true')
25 parser.add_argument('-o', '--out', dest = 'out_file',
26 help='Out img to file (default svg). For auto
date name type -o %%. NOTE:-o option implies
-n')
27 parser.add_argument('-p', '--png', dest = 'format_png',
help='Use png image format', action='store_true')
28 parser.add_argument('-n', '--nodisp', dest = 'no_disp',
help='Dont output to screen', action='store_true')
29 parser.add_argument('-w', '--web', dest = 'do_xra', help
='Add NOAA XRA events', action='store_true')
30 parser.add_argument('-t', '--time', dest = 'add_time',
help='Add timestamp on image',action='store_true')
31 parser.add_argument('-s', '--std', dest = 'std_th', help
='Hide station with standard deviation below threshold
')
32
33 (args, unk) = parser.parse_known_args()
34
35 if args.no_disp:
36 mpl.use('Agg') # Needed when using in no x-server
environment
37 print('[+] Quiet mode selected')
38
39 import matplotlib.pyplot as plt
40
41 #-----
42 filenames = unk
43 #-----
44
45 h_1 = [ 1.622815222112881e-19, 2.742537274305169e-20,
46 0.0001955009058112673, 0.0008122466684707235,
47 0.00167628566755187, 0.001898196354462748,
48 -1.341670764578074e-18, -0.005166904315748217,
49 -0.01286605438689116, -0.01918598132512281,
50 -0.01729947863060609, 5.201490048368725e-18,
51 0.03618254536691876, 0.08742352578244647,
52 0.1420576346227533, 0.1841609822245467,

```

```

53         0.1999999999999869,      0.1841609822245467,
54         0.1420576346227536,      0.08742352578244661,
55         0.03618254536691877,      5.201490048368729e-18,
56         -0.01729947863060611,     -0.01918598132512283,
57         -0.01286605438689118,     -0.005166904315748217,
58         -1.341670764578074e-18,    0.001898196354462752,
59         0.001676285667551872,      0.0008122466684707237,
60         0.0001955009058112676,     2.742537274305191e-20,
61         1.622815222112881e-19]
62
63     h_2 = [ 0,                      3.72273085387742e-05,
64            -0.000534907099040992,  -0.00206020983902134,
65            -0.00271874508434841,    0.000480396001623683,
66            0.00784505469068691,     0.013938827328398,
67            0.00983007278517655,     -0.00888675829469037,
68            -0.033955935832742,      -0.0443157009212781,
69            -0.0173572768752905,      0.0541859333943871,
70            0.151821372334918,        0.236842476419856,
71            0.270563403256189,        0.236842476419856,
72            0.151821372334918,        0.0541859333943901,
73            -0.0173572768752907,      -0.0443157009212784,
74            -0.0339559358327422,     -0.00888675829469115,
75            0.00983007278517606,      0.013938827328398,
76            0.00784505469068691,     0.000480396001623683,
77            -0.00271874508434833,    -0.00206020983902134,
78            -0.000534907099040995,    3.72273085387745e-05,
79            0]
80     M = 6
81
82     class sid_plot:
83
84         def __init__(self, file_obj):
85
86             self.call_sign = 'None'
87             self.start_date = '0000-00-00'
88             self.loginterval = 1
89             self.stations = []
90             self.frequencies = []
91
92             [self.lat, self.lon] = [0.00, 0.00]
93
94             self.file_obj = file_obj
95
96             self.obtain_csv_properties()
97
98         def obtain_csv_properties(self):
99
100             file_obj.seek(0, 0) # Let's go back to the start
101             reader = csv.reader(self.file_obj, delimiter=',')
102             count = 0

```

```

103
104     for line in reader:
105         if line[0][0] == '#': # Header lines start with '#'
106             if line[0].find('Site') > 0:
107                 self.call_sign = line[0][line[0].find('=')+1:].
108                     replace(' ', '')
109                 print('[+] Call signg extracted from file ' +
110                     self.call_sign)
111
112             if line[0].find('UTC_StartTime') > 0:
113                 self.start_date = line[0][18:]
114                 print('[+] Date extracted from file ' + self.
115                     start_date)
116
117             if line[0].find('Longitude') > 0:
118                 self.lon = float(line[0][line[0].find('=')+1:].
119                     replace(' ', ''))
120                 print('[+] Longitude extracted from file ' , self.
121                     .lon)
122
123             if line[0].find('Latitude') > 0:
124                 self.lat = float(line[0][line[0].find('=')+1:].
125                     replace(' ', ''))
126                 print('[+] Latitude extracted from file ' , self.
127                     lat)
128
129             if line[0].find('Stations') > 0:
130                 self.stations = ','.join(line)[line[0].find('=')
131                     +1:].replace(' ', '').split(',')
132                 print('[+] Stations extracted from file ' , self.
133                     stations)
134
135             if line[0].find('Frequencies') > 0:
136                 self.frequencies = ','.join(line)[line[0].find
137                     ('=')+1:].replace(' ', '').split(',')
138                 print('[+] Frequencies extracted from file', self
139                     .frequencies)
140
141             if line[0].find('LogInterval') > 0:
142                 self.loginterval = int(line[0][line[0].find('=')
143                     +1:].replace(' ', ''))
144                 print('[+] Log Interval extracted from file' ,
145                     self.loginterval)
146
147             else:
148                 if count > 3:
149                     break
150
151             count = count+1
152
153     file_obj.seek(0, 0)

```

```

140     return self.call_sign, self.stations, self.frequencies,
        self.start_date, self.lat, self.lon
141
142 def csv_reader(self, file_obj, st_num):
143     col = np.zeros(shape=(24*3600//self.loginterval, 1))
144     reader = csv.reader(file_obj, delimiter=',')
145     count = 0
146
147     file_obj.seek(0, 0) # Let's go back to the start
148     for line in reader:
149         if line[0][0] != '#':
150             col[count] = float(line[st_num])
151             count = count+1
152
153     #col.astype(np.float)
154     a = np.frombuffer(col)
155
156     return a
157
158 def make_plot(self):
159     global h_1, M, h_2
160     fig, ax = plt.subplots() # Only one subplot
161
162     #-----
163     ax.set_axisbelow(True) # Grid below data
164     ax.minorticks_on() # To enable minor grid
165     ax.grid(which = 'major', linestyle="-.") # Major grid
166     ax.grid(which='minor', linestyle='-.', linewidth=0.5) #
        Minor grid
167
168     y_unit = '(Nat)'
169     if args.do_log: y_unit = '(dB)'
170
171     plt.ylabel('Rx power (relative)' + y_unit) # Label on
        rx axis
172     plt.xlabel('UTC time') # Label on time axis
173     # Title = Name+Date(Iso8601)
174     plt.title(self.call_sign+' SID @ '+self.start_date
        [0:10], fontsize=10)
175
176     #-----
177
178     hours = dates.HourLocator(interval=3)
179     dfmt = dates.DateFormatter('%H:%M')
180
181     datemin = datetime(2017, 1, 1, 0, 0)
182     datemax = datetime(2017, 1, 2, 0, 0)
183     ax.xaxis.set_major_locator(hours)
184     ax.xaxis.set_major_formatter(dfmt)
185     ax.set_xlim(datemin, datemax)

```



```

186
187     if args.add_time:
188         ax.text(0.1, 0.9, datetime.now(timezone.utc).strftime
189             ("%H:%M")+ ' UTC',
190             verticalalignment='top', horizontalalignment='
191                 center',
192             transform=ax.transAxes, color='k', fontsize=15,
193             bbox=dict(fill=True, alpha=0.9, facecolor='w'))
194
195     # Dim on night 00-05.5
196     plt.axvspan(datemin, datemin+timedelta(hours = 5.5),
197                 facecolor='k', alpha=0.1)
198     # Dim on night 18.5-24
199     plt.axvspan(datemin+timedelta(hours = 18.5), datemax,
200                 facecolor='k', alpha=0.1)
201
202     #-----
203     d_factor = 1
204     if args.custom:
205         d_factor = M
206     x_data = self._generate_timestamp(d_factor)
207
208     plot_axis = []
209     skip = []
210     [k, offset] = [0, 0]
211     [y_min, y_max] = [[], []]
212
213     while k < len(self.stations):
214         plot_station = True
215         try:
216             y_data = self.csv_reader(self.file_obj, k+offset)
217             y_data[y_data <= 0] = np.NaN # To avoid transient
218                 after last sample
219             if args.custom:
220                 y_data = self.two_phase_fixed_frequency_filter(
221                     y_data, h_1, M, h_2)
222             elif args.filter:
223                 y_data = self.mov_avg(y_data, 6*2+1) # Filter
224                     with moving average
225
226             y_data[y_data <= 0] = np.NaN # To avoid error at
227                 log10
228             if args.do_log: y_data = 20*np.log10(y_data)
229
230             if args.std_th:
231                 if np.nanstd(y_data, ddof=1) < float(args.std_th)
232                     :
233                     plot_station = False
234                     skip.append(k)
235
236

```

```

227     if args.do_log and plot_station:
228         y_min.append(self.min(y_data[100:-100]))
229         y_max.append(self.max(y_data))
230     except:
231         offset = 1 # Will fail for buffers with timestamp
232         k = 0 # Offset is to skip one column
233         continue
234     if plot_station:
235         new_a, = ax.plot(x_data, y_data, alpha = 0.8)
236         plot_axis.append(new_a)
237         k = k+1
238     leg_list = []
239     for i in range(0, len(self.stations)):
240         if i not in skip:
241             leg_list.append(self.stations[i] + ' ('+ '%.2f' % (
                float(self.frequencies[i])/1000)+'kHz)')
242     if args.do_log: ax.set_ylim([self.min(y_min)-1, self.max
        (y_max)+1]) # Logarithmic axis limits
243     plt.legend(plot_axis, leg_list, loc='upper right',
        bbox_to_anchor=(1,1), fontsize = 9) # Add legend to
        plot
244
245     #-----
246
247     if args.do_xra:
248         events_list = self.get_XRA()
249
250         for event in events_list:
251             x_start = datetime(2017,1,1,int(event['Begin
                '][0:2]), int(event['Begin'][2:4]))
252             x_max = datetime(2017,1,1,int(event['Max'][0:2]),
                int(event['Max'][2:4]))
253             x_end = datetime(2017,1,1,int(event['End'][0:2]),
                int(event['End'][2:4]))
254             plt.axvline(x = x_start, color = 'g', alpha = 0.9,
                linestyle = ':')
255             plt.axvline(x = x_max, color = 'r', alpha = 0.9,
                linestyle = ':')
256             plt.axvline(x = x_end, color = 'y', alpha = 0.9,
                linestyle = ':')
257
258             min_axis = 0
259             if args.do_log: min_axis = self.min(y_min)-0.2
260             ax.text(x_max, min_axis, event['Particulars'], bbox
                ={'facecolor':'white', 'alpha':0.5})
261
262     #-----
263
264     if args.out_file: # If argument was provided

```

```

265     fig.set_size_inches(12, 7.5) # (18.5, 10.5) # Set
        image size
266     if args.out_file == '%': # If '%' was provided as
        argument:
267         name = self.call_sign + '_' + self.start_date[0: 10]
            # Then use automatic name
268     else: # If not:
269         name = args.out_file # Use provided name
270
271     img_format = 'svg'
272     if args.format_png: img_format = 'png'
273     plt.savefig( name+'.'+img_format, format=img_format,
        bbox_inches='tight', pad_inches=0.1)
274
275     # If neither out_file nor no_disp was provided
276     elif args.no_disp == False:
277         plt.show() # Show plot
278
279     def min(self, array):
280         l = 0
281         for k in array:
282             if not np.isnan(k) and k!=0:
283                 if l == 0:
284                     current_min = k
285                     l = 1
286                 else:
287                     if k < current_min:
288                         current_min = k
289         return current_min
290
291     def max(self, array):
292         l = 0
293         for k in array:
294             if not np.isnan(k):
295                 if l == 0:
296                     current_max = k
297                     l = 1
298                 else:
299                     if k > current_max:
300                         current_max = k
301         return current_max
302
303     # Two phase filter implementation only to be used with T
        =5sec
304     def two_phase_fixed_frequency_filter(self, array, h_1, M,
        h_2):
305         temp = signal.filtfilt(h_1, 1, array)
306         temp2 = signal.decimate(temp, M)
307         temp2 = signal.filtfilt(h_2, 1, temp2)
308         return temp2

```

```

309
310 def mov_avg(self, array, window = 10):
311     temp = np.zeros(len(array))
312     temp_avg = 0
313     for j in range(0, len(array)-window):
314         for i in range(0, window):
315             temp_avg = temp_avg+array[j+i]
316             temp_avg = temp_avg/window
317             temp[j] = temp_avg
318             temp_avg = 0
319
320     return temp
321
322 def _generate_timestamp(self, M = 0): # Function
323     extracted from supersid_plot.py
324     timestamp = np.empty(24*3600 // self.loginterval // M,
325                          dtype=datetime)
326     interval = timedelta(seconds= int(self.loginterval)*M)
327     currentTimestamp = datetime(2017,1,1,0,0,0)
328     for i in range(len(timestamp)):
329         timestamp[i] = currentTimestamp
330         currentTimestamp += interval
331     return timestamp
332
333 def get_XRA(self):
334     day = self.start_date[0: 10].replace('-', '')
335     NOAA_URL = 'ftp://ftp.swpc.noaa.gov/pub/indices/events
336               /%sevents.txt' % (day)
337     resulttext = b''
338     try:
339         request = urllib.request.Request(NOAA_URL)
340         result = urllib.request.urlopen(request)
341         resulttext = result.read()
342
343     except:
344         print ("[E] In NOAA XRA service")
345
346     XRA_fields = []
347     XRA_list = []
348
349     resulttext = resulttext.decode('UTF-8').split('\n')
350     for each_line in resulttext:
351         if each_line.find('#Event') > -1:
352             XRA_fields = sid_plot._list_replace(each_line.
353                                                  replace('#', '').split(' '), ' ', '')
354
355         if each_line.find('XRA') > -1:
356             each_line = sid_plot._list_replace(each_line.
357                                                  replace('+', '').split(' '), ' ', '') # Double
358             space

```

```

353     temp_dic = {}
354     for k in range(0,len(XRA_fields)): temp_dic[
355         XRA_fields[k]] = each_line[k]
356     XRA_list.append(temp_dic)
357
358     return XRA_list
359
360 def _list_replace(list, del_char, new_char):
361     k = 0
362     l = len(list)
363     while k < l:
364         list[k] = list[k].replace(del_char, new_char)
365         if list[k] == '':
366             list.pop(k)
367             l -= 1
368         else:k += 1
369
370     return list
371
372 #-----
373 if __name__ == "__main__":
374
375     for each_file in filenames:
376         try:
377             with open(each_file, 'r') as file_obj:
378                 ssp = sid_plot(file_obj)
379                 ssp.make_plot()
380         except:
381             pass

```

## 7.10 Results and conclusion

It is clear that the way to prove the correct functioning of the system system would have been to successfully record a flare. In this case it has not been possible, given the quiet conditions of the Sun and the little time that was devoted to testing and measurements (see appendix 1). This makes capturing a flare mostly a matter of luck. However, having registered the day-night cycle variations proves that the system does indeed work, as these are produced due to the daily changes in the ionosphere.

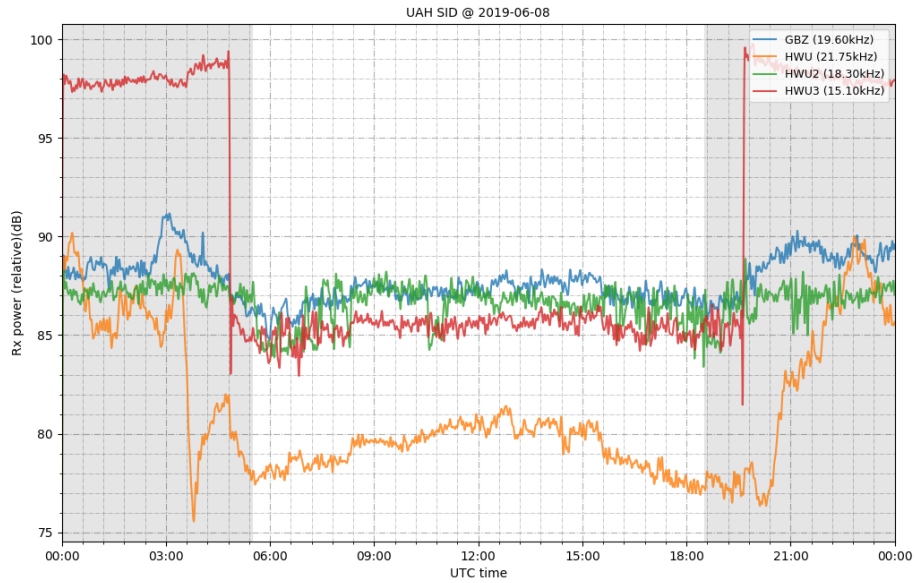


Figure 37: Custom filtered data obtained during the 8<sup>th</sup> of June

Figure 37 condenses everything that has been done in one image. To produce it, the theory behind each of the elements of the system has been developed, and hardware and software tools have been designed and built. This graph also shows a noticeable improvement over the moving average filter featured in figure 29 and a massive difference when compared to the raw data.

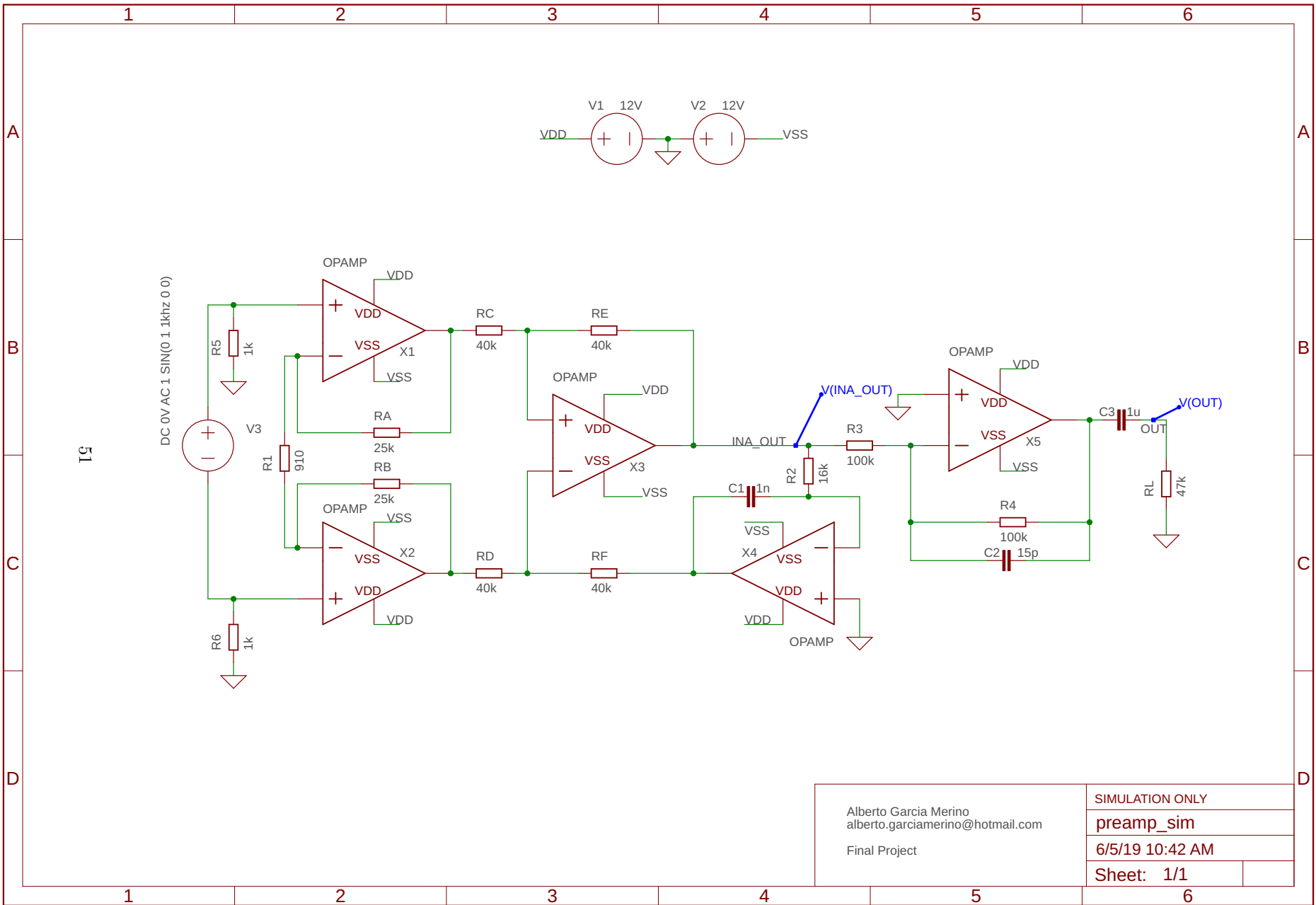
In addition, a web page ([www.spaceweather.es/sid](http://www.spaceweather.es/sid)) has been brought up where daily plots of the data dumps for several stations are publicly available, as well as a self updating plot of the present day.

## 8 Blueprints and diagrams

Schematic designs are given for the preamplifier and power supply described in section 7.7, as well as the PCB design for each of them. The included layered board exports allow for construction using photographic PCB making methods as they are given with a 1:1 scale.

The designs featured in this section are:

- Page 50 - Preamplifier simulation schematic
- Page 51 - Preamplifier design schematic
- Page 52 - Preamplifier PCB layers
- Page 53 - Power supply design schematic
- Page 54 - Power supply PCB layers



Alberto Garcia Merino  
 alberto.garciamerino@hotmail.com  
 Final Project

SIMULATION ONLY  
 preamp\_sim  
 6/5/19 10:42 AM  
 Sheet: 1/1



1 2 3 4 5 6

A

A

B

B

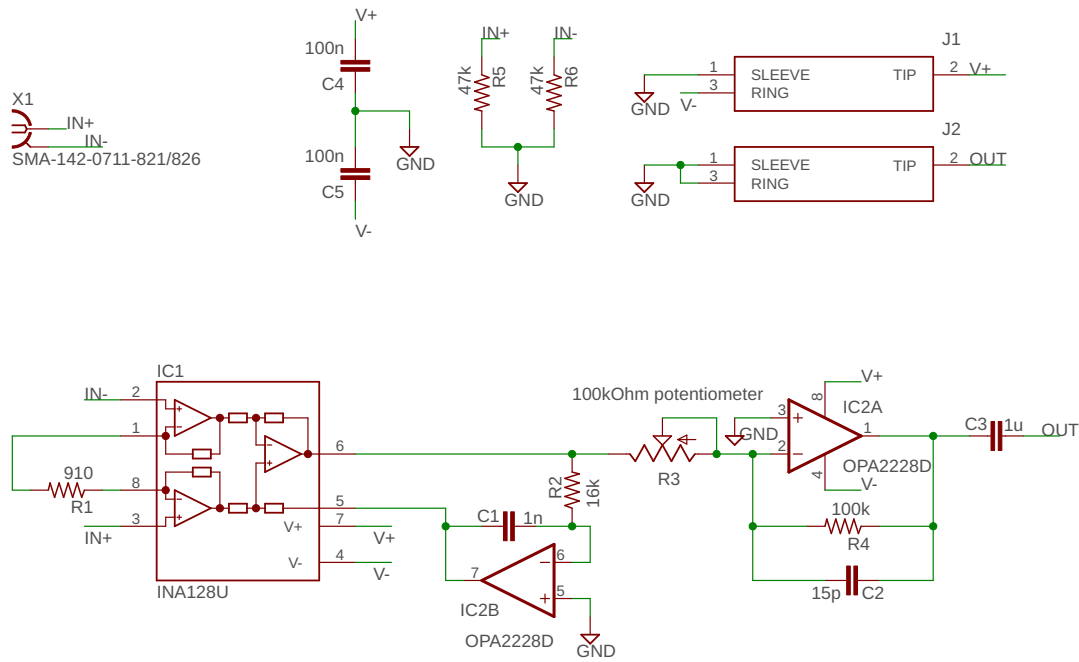
C

C

D

D

52



Values are computed for 35 to 55dB (100k to 10k pot) gain and 10kHz-106kHz bandwidth. Refer to documentation for design equations.

Alberto Garcia Merino alberto.garciamerino@hotmail.com  Final project	preamp	
	6/5/19 10:01 AM	
	Sheet: 1/1	

1 2 3 4 5 6

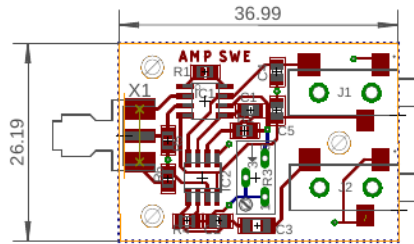


Figure 38: Preamplifier PCB

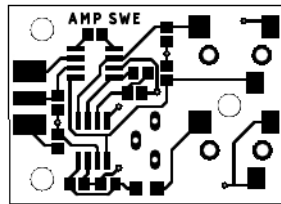


Figure 39: Top layer

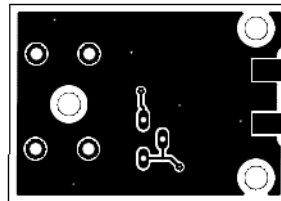


Figure 40: Bottom layer

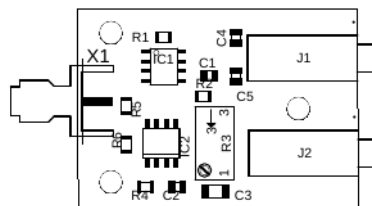
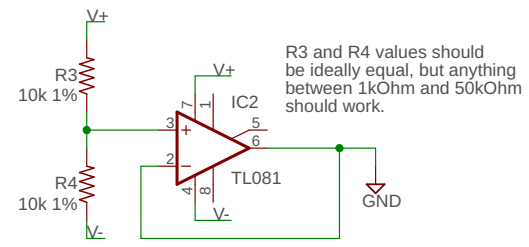
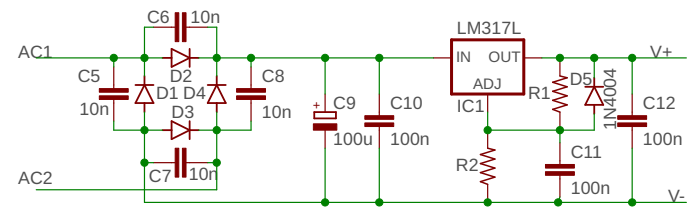
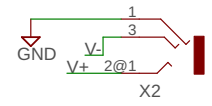
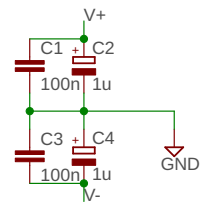
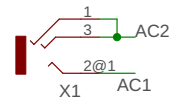
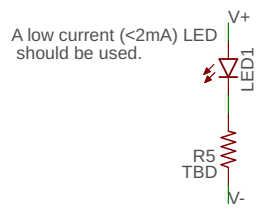


Figure 41: Placement



Alberto Garcia Merino alberto.garciamerino@hotmail.com	
Final project	
power_supply	
6/9/19 11:25 AM	
Sheet: 1/1	

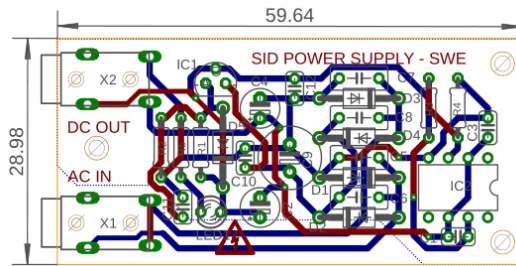


Figure 42: Power supply PCB

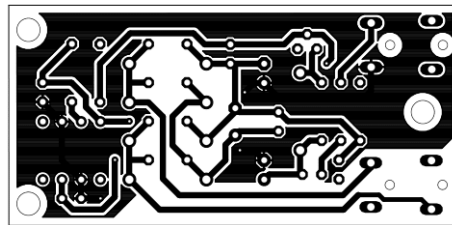


Figure 43: Top layer

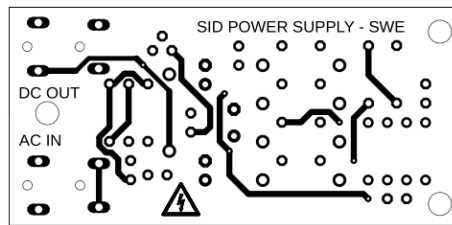


Figure 44: Bottom layer

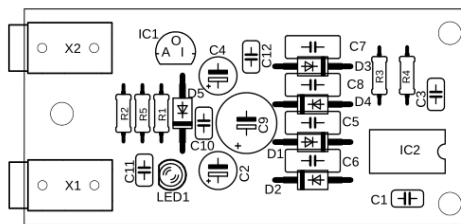


Figure 45: Placement

## 9 Budget and bill of materials

In the following tables (tables 2 to 8) the total cost of the project is broken down in several categories. These account not only for the materials cost but also for fees cost and the amortization of software and hardware tools. Additionally, as the antenna was commissioned to a woodworking workshop, its cost is shown apart from the rest.

In the case of hardware, the amortization is computed as a four year period, from which the hours devoted to this project determine its value. For software the same process is followed, with the difference that the cost of it spans a year as determined by the provider.

Due to the impossibility to show the tables of each section, for their size and amount, the total budget summary is shown here, in table 2, and it is broken down in tables 3 to 8 on the next pages.

Concept	Cost
Materials	190.39€
PCB workshop use	28.00€
Woodworking fees	1600.00€
Professional fees	9600.00€
Software amortization	225.00€
Hardware amortization	25.00€
<b>TOTAL</b>	<b>11,668.39€</b>

Table 2: Budget

Finally, the total cost of the project is estimated as 11,668.39€.

Concept	Quantity	Price
Resistor THT 430R	1	0.03€
Resistor THT 3k9	1	0.03€
Resistor THT 10k	3	0.09€
Resistor 910R SMD 0805	1	0.02€
Resistor 16k SMD 0805	1	0.02€
Resistor 100k SMD 0805	1	0.02€
Resistor 47k SMD 0805	2	0.04€
Multi turn potentiometer 100k	1	1.00€
Electrolytic capacitor 1uF 63V	2	0.26€
Electrolytic capacitor 100uF 35V	1	0.20€
Ceramic capacitor 10nF 50V	4	0.32€
Ceramic capacitor 100nF 50V	5	0.50€
Capacitor SMD 0805 15pF	1	0.27€
Capacitor SMD 0805 1nF	1	0.31€
Capacitor SMD 0805 100nF	2	0.88€
Capacitor SMD 1206 1uF	1	0.66€
Diode 1N4001	5	0.30€
LED 3mm green	1	0.10€
DIP8 socket	1	0.25€
LM317L	1	0.82€
TL081	1	0.74€
OPA2228U dual OPAMP	1	5.50€
INA128U instrumentation AMP	1	8.10€
Jack 3.5 mm female 3 pole THT [1267376] <sup>a</sup>	2	6.62€
Jack 3.5 mm female 3 pole SMD [2839854] <sup>a</sup>	2	2.81€
Jack 3.5 mm male 3 pole 90° cable	2	2.58€
Jack 3.5 mm male 2 pole cable	4	3.98€
Jack 3.5 mm female 2 pole cable	1	1.10€
SMA female PCB straight side mount	1	7.83€
SMA male cable mount RG-58	1	6.32€
Fuse 80 mA	2	0.32€
Fuse holder panel mount	1	2.94€
Transformer 12VAC (Repurposed)	1	0.00€
Coaxial cable RG-58	8m	10.88€
Three wire audio cable	2m	1.30€
Dual audio/video cable	20m	13.35€
Solid core tinned copper wire 23 AWG	300m	67.20€
FR4 double sided board 100x160 mm	1	9.66€
<b>TOTAL</b>		<b>157.35€</b>
<b>TAX(21%)</b>		<b>33.04€</b>
<b>TOTAL+TAX</b>		<b>190.39€</b>

<sup>a</sup>Farnell code is provided for those connectors that must match the PCB footprint

Table 3: Materials

Concept	Use	Cost rate	Cost
LPKF milling machine	4 h	7€/hour	28.00€
<b>TOTAL</b>			<b>28.00€</b>

Table 4: PCB construction

Concept	Cost
Materials (Iroko Wood)	400.00€
Carpenter fees	1200.00€
<b>TOTAL</b>	<b>1600.00€</b>

Table 5: Antenna structure construction

Task	Hours	Cost rate	Cost
Engineering design	190	40€/h	7600€
Documentation	70	20€/h	1400€
Construction	40	15€/h	600€
<b>TOTAL</b>			<b>9600€</b>

Table 6: Professional fees

Tool	Category	Cost rate	Cost
Eagle PCB standard	PCB design and sim.	100€/year	15€
Matlab+Toolbox	Data processing	1200€/year	210€
Linux	Operating system	0€/year	0€
VS Code	Latex editor	0€/year	0€
Latex	Document preparation	0€/year	0€
<b>TOTAL</b>			<b>225€</b>

Table 7: Software amortization

Tool	Cost
Acer aspire E15 i5-5200U 4GB RAM	25€
<b>TOTAL</b>	<b>25€</b>

Table 8: Hardware amortization

## 10 User manual and setup guide

This section provides a step by step guide to get the system up and running. Hardware setup as well as software tools are covered along with their basic configuration.

### 10.1 Hardware

There are three main pieces of hardware in the system:

- Antenna
- Amplifier and supply
- Computer

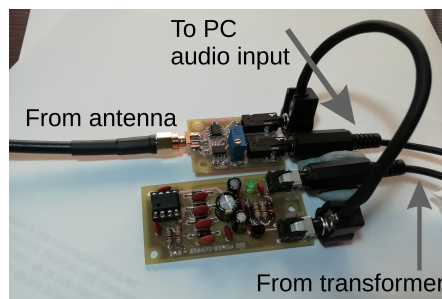


Figure 46: Amplifier and supply setup

If the design given in section 8 is used, the antenna must be terminated with a male SMA connector, which connects to the amplifier input as shown in figure 46. Then, after connecting the supply output to the amplifier through a short audio cable, the remaining cables can be plugged. One of them powers the whole setup, as it is connected to the transformer secondary coil, while the other serves as a signal return path and should be connected to the computer audio input jack.

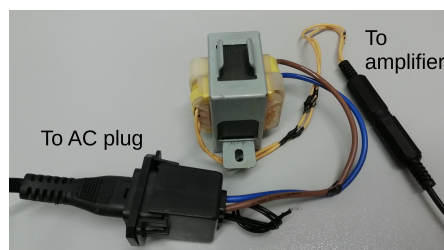


Figure 47: Transformer



The transformer that powers the boards should follow the configuration shown in figure 47. For protection, a 50mA to 200mA fuse must be soldered in series with the primary of the transformer.

These connections must be done carefully, as any error may damage the boards. As an additional level of precaution, it is advised to power everything up after all the connections have been made and verified.

With regards to the amplifier, its gain should be reduced to its minimum as the output may saturate. Then, with the aid of the logging software it can be tuned to fit the needs of the station.

## 10.2 Software

Due to the flexibility it provides and its ease of use, a Debian based Linux distribution is recommended. Though there are many, Lubuntu is a good example, as it uses a lightweight desktop environment.

In it, the required dependencies to run the software must be satisfied. In the following lines an example installation script is shown.

```
sudo apt update
sudo apt upgrade

sudo apt install git python python-alsaudio screen python3
python3-numpy python3-scipy python3-matplotlib
```

Then, the logging software provided by EricGibert (SuperSID) can be cloned from its GitHub repository.

```
git clone https://github.com/ericgibert/supersid.git
```

This will download a series of files. All the scripts are stored under the *supersid* folder. Then, the script that lists the sound devices will have to be run. This will show which sound cards are available.

```
python sampler.py
```

The aforementioned script will produce an output similar to the one shown below.

```
Accessing PCH ...
alsaudio sound card capture on sysdefault:CARD=PCH at
48000 Hz
48000 bytes read from alsaudio sound card capture on
sysdefault:CARD=PCH (48000,)
[18239 18228 18221 18200 18200 18203 18211 18219 18184
18184]
Vector sum 147966762
alsaudio sound card capture on sysdefault:CARD=PCH at
96000 Hz
```

```
96000 bytes read from alsaaudio sound card capture on
  sysdefault:CARD=PCH (96000,)
[0 0 0 0 0 0 0 0 0 0]
Vector sum 144350
```

From it, the name of the sound card should be annotated, as it is required in the configuration file. In this case the used sound card is labeled PCH. It can be seen that the PCH device can only sample below 48 kHz, as no output is returned at 96 kHz.

Now, the main configuration file has to be edited. It is stored under the *Config* directory, and contains not only the sampling parameters, but also the frequencies to be monitored. The sound card device name has to be specified in the *Card* parameter and the data folder in the *data\_path* parameter. This directory must be created in advance, otherwise the program will not run.

An example *supersid.cfg* is provided below.

```
1 [PARAMETERS]
2 viewer = text
3 site_name = UAH
4 monitor_id = UAH
5 contact = sample@email.net
6
7 longitude = -3.4016954
8 latitude = 40.4947846
9 utc_offset = +01:00/+02:00
10 time_zone = CET/CEST
11 audio_sampling_rate = 48000
12
13 log_interval = 5
14 log_format=sid_format
15 log_type = filtered
16 scaling_factor = 1.0
17
18 # Change path to data directory
19 hourly_save = YES
20 data_path = /home/sid-uah/Desktop/supersid/Data
21 number_of_stations = 3
22
23 #-- STATIONS --
24 [STATION_1]
25 call_sign = GBZ
26 color = y
27 frequency = 19600
28
29 [STATION_2]
30 call_sign = NWC
31 color = y
32 frequency = 19800
33
34 [STATION_3]
```

```

35 | call_sign = ICV
36 | color = y
37 | frequency = 20270
38 |
39 | #-- DEVICE --
40 | [Capture] # Change device name
41 | Audio=alsaudio
42 | Card=PCH
43 | PeriodSize = 512
44 |
45 | [FTP] # Disabled
46 | automatic_upload = no
47 | ftp_server = sid-ftp.stanford.edu
48 | ftp_directory = /incoming/SuperSID/NEW/
49 | local_tmp = /tmp
50 | call_signs = UAH

```

Finally, the logging software can be executed. It is recommended to run it under *screen* or *tmux*, as it allows to launch it from an SSH session and be left running on the background after logout.

```
| screen python supersid.py
```

Now, the data will be periodically dumped to files under the specified data directory and can be plotted using the plotter script developed in this project. The GitHub repository can be cloned with the following command.

```
| git clone https://github.com/AlbertoGM97/sid_plot.git
```

And then can produce output image plots with the following arguments.

```
| python3 sid_plot.py hourly_current_buffers.raw.ext
   .2019-06-14.csv -o % -n -p -c -l -w
```

It should be noted that the dump files are low in entropy (below  $3.8 \text{ bit B}^{-1}$ ) and can be easily compressed to save space using tools such as zip or 7z.

## 11 Appendix 1

Using an early prototype with similar characteristics to the one described in this project a flare was successfully recorded. This C class flare produced on the 6<sup>th</sup> of May of 2019 disturbed the ionosphere above the great circle path between Alcalá de Henares (Spain) and Isola di Tavolara (Italy), which produced a sudden enhancement in the received power of the ICV transmitter.

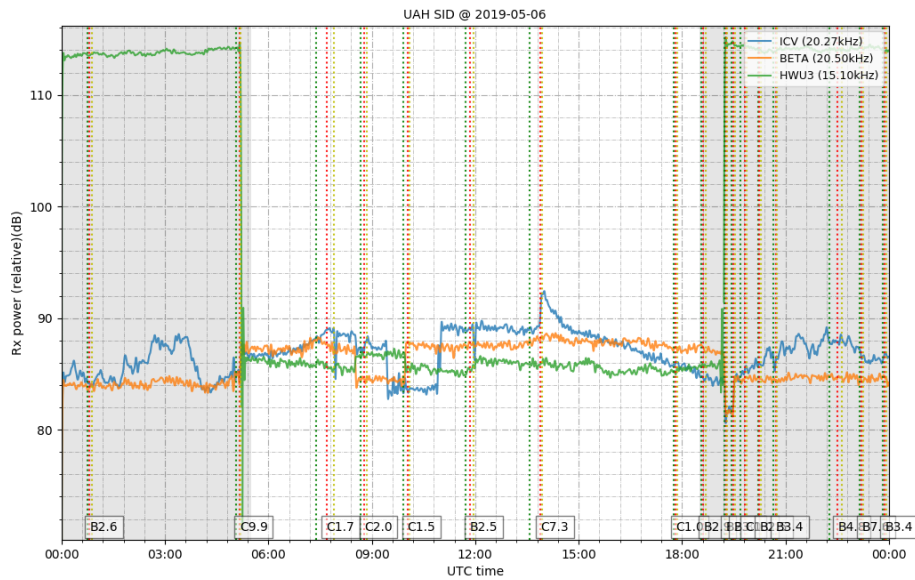


Figure 48: Log captured in the 6<sup>th</sup> of May

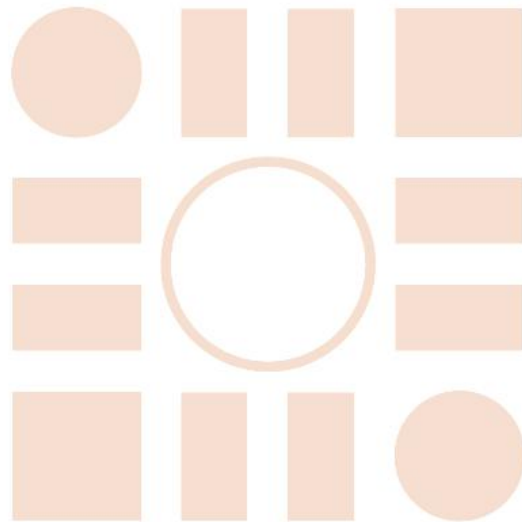
## References

- [1] R. C. Carrington, “Description of a singular appearance seen in the sun on september 1, 1859,” *Monthly Notices of the Royal Astronomical Society*, vol. 20, pp. 13–15, 1859.
- [2] R. J. Redmon, D. B. Seaton, R. Steenburgh, J. He, and J. V. Rodriguez, “September 2017’s geoeffective space weather and impacts to caribbean radio communications during hurricane response,” *Space Weather*, vol. 16, no. 9, pp. 1190–1201, 2018.
- [3] A. O. Benz, “Flare observations,” *Living reviews in solar physics*, vol. 14, no. 1, p. 2, 2017.
- [4] Y. Kamide and A. C.-L. Chian, *Handbook of the solar-terrestrial environment*. Springer Science & Business Media, 2007.
- [5] M. Nicolet and A. Aikin, “The formation of the d region of the ionosphere,” *Journal of Geophysical Research*, vol. 65, no. 5, pp. 1469–1483, 1960.
- [6] R. Fitzpatrick, “Dielectric constant of a plasma,” 2006.
- [7] J. R. Wait and K. P. Spies, *Characteristics of the Earth-ionosphere waveguide for VLF radio waves*. No. 300, US Dept. of Commerce, National Bureau of Standards: for sale by the Supt. of . . . , 1964.
- [8] W. M. McRae and N. R. Thomson, “Solar flare induced ionospheric d-region enhancements from vlf phase and amplitude observations,” *Journal of Atmospheric and Solar-Terrestrial Physics*, vol. 66, no. 1, pp. 77–87, 2004.
- [9] K. J. Lynn, “Vlf waveguide propagation: The basics,” in *AIP Conference Proceedings*, vol. 1286, pp. 3–41, AIP, 2010.
- [10] “Prediction of field strength at frequencies below about 150 khz,” *ITU-R P.684, International Telecommunication Union*, 2016.
- [11] “Ground-wave propagation curves for frequencies between 10 khz and 30 mhz,” *ITU-R P.368, International Telecommunication Union*, 2007.
- [12] R. Bracewell, T. Straker, and R. Redman, “The study of solar flares by means of very long radio waves,” *Monthly Notices of the Royal Astronomical Society*, vol. 109, no. 1, pp. 28–45, 1949.
- [13] J. Kraus, “Antennas,” 1950.
- [14] F. W. Grover, *Inductance calculations: working formulas and tables*. Courier Corporation, 2004.
- [15] R. D. Straw, “The arrl antenna book: the ultimate reference for amateur radio antennas, transmission lines and propagation,” *Editorial Amer Radio Relay League (ARRL). Edición*, vol. 21, 2003.
- [16] “Radio noise,” *ITU-R P.372, International Telecommunication Union*, 2016.
- [17] J. S. Barlow, G. W. Frey Jr, and J. B. Newman, “Very low frequency noise power from the lightning discharge,” *Journal of the Franklin Institute*, vol. 258, no. 3, pp. 187–203, 1954.

- [18] C. E. Shannon, “Communication in the presence of noise,” *Proceedings of the IEEE*, vol. 86, no. 2, pp. 447–457, 1998.
- [19] H. T. Friis, “Noise figures of radio receivers,” *Proceedings of the IRE*, vol. 32, no. 7, pp. 419–422, 1944.
- [20] M. B. Velasco, F. C. Roldán, R. J. Martínez, and J. S. Landete, *Tratamiento digital de señales*. Servicio de Publicaciones. Universidad de Alcalá, 2013.



Universidad de Alcalá  
Escuela Politécnica Superior



ESCUELA POLITECNICA  
SUPERIOR



Universidad  
de Alcalá